

## DATA ANALYSIS METHODS FOR THE DETECTION OF THE EPOCH OF REIONIZATION

CARINA CHENG<sup>1</sup>, AARON R. PARSONS<sup>1,2</sup>, MATTHEW KOLOPANIS<sup>3</sup>, DANIEL C. JACOBS<sup>3</sup>, SAUL A. KOHN<sup>4</sup>, ADRIAN LIU<sup>1,5</sup>,  
 JAMES E. AGUIRRE<sup>5</sup>, ZAKI S. ALI<sup>1</sup>, RICHARD F. BRADLEY<sup>6,7,8</sup>, GIANNI BERNARDI<sup>9,10,11</sup>, CHRIS L. CARILLI<sup>12,13</sup>, DAVID R.  
 DEBOER<sup>2</sup>, MATTHEW R. DEXTER<sup>2</sup>, JOSHUA S. DILLON<sup>1</sup>, PAT KLIMA<sup>7</sup>, DAVID H. E. MACMAHON<sup>2</sup>, DAVID F. MOORE<sup>5</sup>,  
 CHUNEETA D. NUNHOKEE<sup>14</sup>, JONATHAN C. POBER<sup>15</sup>, WILLIAM P. WALBRUGH<sup>9</sup>, ANDRE WALKER<sup>9</sup>

<sup>1</sup>Astronomy Dept., U. California, Berkeley, CA

<sup>2</sup>Radio Astronomy Lab., U. California, Berkeley CA

<sup>3</sup>School of Earth and Space Exploration, Arizona State U., Tempe AZ

<sup>4</sup>Dept. of Physics and Astronomy, U. Penn., Philadelphia PA

<sup>5</sup>Berkeley Center for Cosmological Physics, Berkeley, CA

<sup>6</sup>Dept. of Electrical and Computer Engineering, U. Virginia, Charlottesville VA

<sup>7</sup>National Radio Astronomy Obs., Charlottesville VA

<sup>8</sup>Dept. of Astronomy, U. Virginia, Charlottesville VA

<sup>9</sup>Square Kilometer Array, S. Africa, Cape Town South Africa

<sup>10</sup>Dept. of Physics and Electronics, Rhodes University

<sup>11</sup>Harvard-Smithsonian Cen. for Astrophysics, Cambridge MA

<sup>12</sup>National Radio Astronomy Obs., Socorro NM

<sup>13</sup>Cavendish Lab., Cambridge UK

<sup>14</sup>Dept. of Physics and Electronics, Rhodes University, Grahamstown South Africa

<sup>15</sup>Dept. of Physics, Brown University, Providence RI

### ABSTRACT

The Epoch of Reionization (EoR) is an uncharted era in our Universe’s history during which the birth of the first stars and galaxies led to the ionization of neutral hydrogen in the intergalactic medium. There are many experiments investigating the EoR by tracing the 21 cm line of neutral hydrogen, a signal which is very faint and difficult to isolate. With a new generation of instruments and a statistical power spectrum detection in our foreseeable future, it has become increasingly important to develop techniques that help maximize sensitivity and validate results. Additionally, it is imperative to understand the trade-offs between different methods and their effects on common power spectrum themes. In this paper, we focus on three major themes — signal loss, power spectrum error bar estimation, and bias in measurements. We describe techniques that affect these themes using both a toy model and data taken by the 64-element configuration of the Donald C. Backer Precision Array for Probing the Epoch of Reionization (PAPER). In particular, we highlight how detailed investigations of these themes have led to a revised, higher 21 cm power spectrum upper limit from PAPER-64. This revised result mostly stems from an updated signal loss calculation for loss associated with empirically estimated covariances, and we consider this limit to supersede previously published PAPER-64 and PAPER-32 results.

### 1. INTRODUCTION

By about one billion years after the Big Bang ( $z \sim 6$ ), the very first stars and galaxies are thought to have ionized all the neutral hydrogen that dominated the baryonic matter content in the Universe. This transition period, during which the first luminous structures formed from gravitational collapse and began to emit intense radiation that ionized the cold neutral gas into a plasma, is known as the epoch of reionization (EoR). The EoR is a relatively unexplored era in our cosmic dawn. Its history encodes important information regarding the nature of the first galaxies and the processes of structure formation. Direct measurements of the EoR would unlock

powerful information about the intergalactic medium, revealing connections between the smooth matter distribution exhibited via cosmic microwave background (CMB) studies and the highly structured web of galaxies we observe today.

One promising technique to probe the EoR is to target the 21 cm wavelength emission that is emitted by neutral hydrogen via its spin-flip transition. This technique is powerful because it can be observed as a function of redshift — that is, the wavelength of the signal reaching our telescopes can be directly mapped to a distance from where the emission originated before stretching out as it traveled through expanding space. Tracing the 21 cm line as a function of redshift offers a window into the

evolution of ionization, temperature, and density fluctuations during this transformative era.

Although a detection of the EoR remains elusive, there are several radio telescope experiments that have succeeded in using the 21 cm signal from hydrogen to place constraints on the brightness of the EoR. Examples of experiments investigating the mean brightness temperature of the EoR relative to the CMB are the Experiment to Detect the Global EoR Signature (EDGES; [Bowman & Rogers 2010](#)), the Long Wavelength Array (LWA; [Ellingson et al. 2009](#)), the Large Aperture Experiment to Detect the Dark Ages (LEDA; [Greenhill & Bernardi 2012](#)), the Dark Ages Radio Explorer (DARE; [Burns et al. 2012](#)), the Sonda Cosmológica de las Islas para la Detección de Hidrógeno NeutroSciHi (SCI-HI; [Voytek et al. 2014](#)), the Broadband Instrument for Global Hydrogen Reionisation Signal (BIGHORNS; [Sokolowski et al. 2015](#)), and the Shaped Antenna measurement of the background Radio Spectrum (SARAS; [Patra et al. 2015](#)). Radio interferometers which seek to measure statistical power spectra include the Giant Metre-wave Radio Telescope (GMRT; [Paciga et al. 2013](#)), the LOw Frequency ARray (LOFAR; [van Haarlem et al. 2013](#)), the Murchison Widefield Array (MWA; [Tingay et al. 2013](#)), the 21 Centimeter Array (21CMA; [Peterson 2004](#); [Wu 2009](#)), and PAPER ([Parsons et al. 2010](#)). The Hydrogen Epoch of Reionization Array (HERA), which is currently being built, is a next-generation instrument that aims to combine lessons learned from previous experiments and is forecasted to be able to make a successful high-significance power spectrum detection with an eventual 350 elements using current analysis techniques ([DeBoer et al. 2017](#); [Pober et al. 2014](#)).

The major challenge that faces all 21 cm experiments is isolating a small signal that is buried underneath foregrounds and instrumental systematics that are, when combined, 4-5 orders of magnitude brighter. A clean measurement therefore requires an intimate understanding of the instrument and a rigorous study of data analysis choices. With continual progress being made in the field and HERA on the horizon, it is becoming increasingly important to understand how the methods we choose interact with each other to affect power spectrum results. More specifically, it is imperative to develop techniques and tests that ensure the accuracy and reliability of a potential EoR detection. In this paper, we discuss three themes that are essential to investigate for a robust 21 cm power spectrum analysis. We also highlight four power spectrum techniques and their trade-offs, traps, and connections to the themes. We first approach the themes from a broad perspective, and then perform a detailed case study using data from the 64-element configuration of PAPER, motivating a revised PAPER-64 21 cm power spectrum from the lessons learned.

This paper is organized into two main sections. In Section 2 we introduce the three themes of our focus, using a toy model to develop intuition for each one.

In Section 3 we present a case study into each theme using data from the PAPER-64 array, highlighting key changes from [Ali et al. \(2015\)](#) which have led to a revised PAPER-64 power spectrum result ([[CC: cite retraction or kolopanis paper](#)]). We conclude in Section 4.

## 2. POWER SPECTRUM THEMES AND TECHNIQUES

There are many choices a data analyst must consider. How can time-ordered measurements be combined? How can the variance of the data be estimated? In what way(s) can the data be weighted to suppress contaminated modes while not destroying an EoR signal? How can the source of a detection be properly identified? Many common techniques, such as averaging data, weighting, bootstrapping, and jackknife testing, address these issues but harbor additional trade-offs. For example, an aggressive filtering method may succeed in eliminating interfering systematics but comes at the cost of losing some EoR signal. A chosen weighting scheme may maximize sensitivity but fail to suppress foregrounds.

Despite there being many data analysis choices, measuring the statistical 21 cm power spectrum ultimately requires robust methods for determining accurate confidence intervals and rigorous techniques to identify and suppress systematics. In this paper, we focus on three 21 cm power spectrum themes that encapsulate this goal and discuss four techniques that interplay with each other and impact the themes. We will give brief definitions now, and build intuition for each theme in the sections to follow.

### Power Spectrum Themes

A deep understanding of the following three themes is essential for the accuracy and interpretation of a 21 cm power spectrum result. Stemmed from a re-analysis of PAPER-64 data, we believe these themes serve as an important check-list for a rigorous power spectrum analysis.

- **Signal Loss** (Section 2.1): As explained in the next section, certain analysis techniques can lead to the loss of the EoR signal. If not corrected for, it could lead to a false non-detection. Computing signal loss correctly has subtle challenges but is necessary to ensure the accuracy of any result. PAPER’s analysis is not the first to underestimate loss; results from the GMRT ([Paciga et al. 2013](#)) were also revised from new signal loss calculations associated with their singular value decomposition foreground filter.
- **Error Bar Estimation** (Section 2.2): Confidence intervals on the 21 cm power spectrum result determine the difference between a detection and a null result, which have two very different implications. Errors can be estimated in a variety of ways, and we will discuss a few of them.

- **Bias** (Section 2.3): There are several possible sources of positive power offset in a visibility measurement that can show up as a detection in a power spectrum, such as bias from noise and foregrounds. In particular, a successful EoR detection would also imitate a bias. Proving a bias is EoR may be the most difficult challenge for 21 cm analyses, as it is crucial to be able to distinguish a detection of foreground leakage, for example, from that of EoR. In this paper we will highlight some sources of bias, discuss ways to mitigate their effects, and describe tests that a true EoR detection must pass.

### Power Spectrum Techniques

The following techniques each have advantages when it comes to maximizing sensitivity and understanding systematics in data. However, some have limitations, and we will discuss circumstances in which there are trade-offs. We choose to focus on these four techniques because they represent major steps in PAPER’s power spectrum pipeline, with several of them also being standard steps in general 21 cm analyses.

- **Fringe-rate filtering:** Fringe-rate filtering is an averaging scheme for time-ordered data (Parsons et al. 2016), and we explain the trade-offs of filtering in more detail in Section 2.1. Broadly, a fringe-rate filter increases the sensitivity of a dataset and reduces the number of independent samples by an amount dependent on the width of the averaging window. However, it can also affect the presence of foregrounds and systematics.
- **Weighting:** A dataset can be weighted to emphasize certain spectral features and minimize others. One particular flavor of weighting is inverse covariance weighting, which is a generalized version of inverse variance weighting that also takes into account data correlations. This weighting has the effect of down-weighting correlated information (i.e. foregrounds) and up-weighting noise-like information (i.e. EoR). However, a challenge of inverse covariance weighting is in accurately defining a covariance matrix that best describes the data.
- **Bootstrapping:** Because theoretical models for covariance matrices are questionable and theoretical error estimation methods rely on assumptions that can be violated by data, applying theoretical errors to a 21 cm measurement is often avoided. Hence, bootstrapping is a useful method for estimating errors of a dataset from itself. By randomly drawing many samples of the data, we obtain a sense of its inherent variance, though there are subtleties to consider such as the independence of values in a dataset.
- **Jackknife testing:** A resampling technique useful for estimating bias, jackknives can be taken

along different dimensions of a dataset to cross-validate results. In particular, null tests can be used to verify whether results are free of systematics (Keating et al. 2016). An EoR detection must pass jack-knife and null tests.

In the next three subsections, we study each theme in depth, focusing on how power spectrum technique trade-offs affect each. We use a toy data model to develop intuition into why certain analysis choices may be appealing and discuss ways in which they are limited. We highlight problems that can arise regarding each theme and offer suggestions to mitigate the issues. Ultimately, we show that rigorous investigations into signal loss, error estimation, and bias must be considered for robust 21 cm results.

### 2.1. Signal Loss

In this section we illustrate how signal loss arises in analysis. Signal loss refers to attenuation of the target cosmological signal in a power spectrum estimate. It can arise in a variety of ways in the analysis pipeline, such as fitting a polynomial during spectral calibration, applying a delay-domain filter, or by weighting data by itself. Here we focus on signal loss associated with applying a weighting matrix to data, a loss that can be significant depending on the choice of weighting and one that was previously underestimated in the PAPER-64 analysis.

Driven by the need to mitigate foreground bias, we use a weighting method that succeeds in down-weighting foregrounds. We apply this weighting to data and propagate it into a final estimator using the power spectrum estimation technique of optimal quadratic estimators (OQE; Liu & Tegmark 2011; Liu et al. 2014b). Before showing how signal loss can arise when using different weighting matrices, we first summarize OQE as follows.

We begin with our data vector,  $\mathbf{x}$  which contains our measured visibilities in Jy. It has length  $(N_t, N_f)$ , where  $N_t$  is the number of time integrations and  $N_f$  is the number of frequency channels. Visibilities are measurements of the Fourier transform of the sky along 2 spatial dimensions, and since we are interested in 3-dimensional Fourier-modes we only need to take one Fourier transform of our data along the line-of-sight dimension. We do this when forming the un-normalized power spectrum estimate  $\hat{q}_\alpha$ :

$$\hat{q}_\alpha = \frac{1}{2} \mathbf{x}^\dagger \mathbf{R} \mathbf{Q}^\alpha \mathbf{R} \mathbf{x} \quad (1)$$

The matrix  $\mathbf{Q}$  is an operator that takes our frequency-domain visibilities and Fourier-transforms them into power spectrum space, while also taking into account physical constants such as the Boltzmann constant used to convert Jy to Kelvin. The index  $\alpha$  denotes a waveband in  $k_\parallel$ , where  $k_\parallel$  is the Fourier-dual to frequency under the delay approximation (Parsons et al. 2012).  $\mathbf{R}$  is a weighting matrix — as an example, inverse covariance weighting would set  $\mathbf{R} = \mathbf{C}^{-1}$  and an unweighted case would use  $\mathbf{R} = \mathbf{I}$ , the identity matrix.

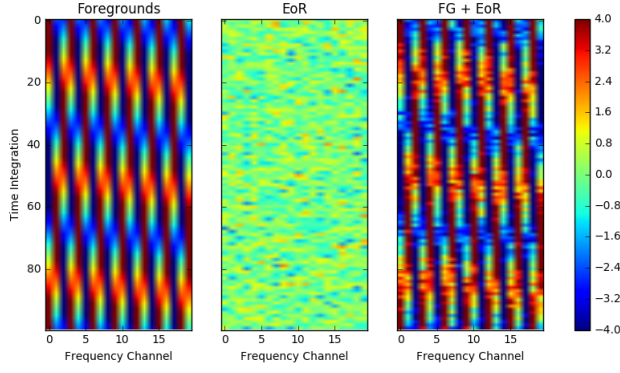


**Figure 1.** Our toy model dataset contains a sinusoid foreground that varies in time and frequency and a random Gaussian signal as a mock EoR signal. Real parts are shown here.

We normalize our power spectrum estimates using the matrix  $\mathbf{M}$ :

$$\hat{\mathbf{p}} = \mathbf{M}\hat{\mathbf{q}}, \quad (2)$$

where  $\hat{\mathbf{p}}$  is the normalized estimate of the true power spectrum. The data analyst has a choice for  $\mathbf{M}$ . For simplicity in this section we set  $\mathbf{M} \propto \mathbf{I}$ , although we explore other cases for the analysis of PAPER-64 data as explained in Section 3.3

In the next sections, we investigate the effects of weighting matrices on signal loss by experimenting with different matrices  $\mathbf{R}$  and examine their impact on the resulting power spectra estimate  $\hat{\mathbf{p}}$ . Our ultimate goal in experimenting with weighting is to suppress foregrounds and investigate EoR losses associated with it.

#### 2.1.1. Toy Model: Inverse Covariance Weighting

To build our intuition into how a particular choice of weighting, namely inverse covariance weighting, can lead to signal loss, we use a toy model. We construct a simple dataset that contains 2-dimensional data (representing visibility data with 100 time integrations and 20 frequency channels). This model represents realistic dimensions of about an hour of PAPER data which might be used for a power spectrum analysis. For PAPER-64 we use  $\sim 8$  hours of data for our analysis, but here we scale it down for this toy model with no loss of generality. We create a mock bright foreground signal,  $\mathbf{x}_{FG}$ , as a complex sinusoid with a fixed frequency and a smoothly varying offset in time, a simplistic but realistic representation of a single bright source. We also create a mock EoR signal,  $\mathbf{x}_{EoR}$ , as a complex, Gaussian random signal [CC: need to motivate why, since real EoR does have correlations]. Our combined data vector is  $\mathbf{x} = \mathbf{x}_{FG} + \mathbf{x}_{EoR}$ , to which we apply different weighting schemes. The three data vectors are shown in Figure 1.

One choice for the weighting matrix  $\mathbf{R}$  is an inverse covariance matrix. This type of weighting is attractive for power spectrum analyses because it is an aggressive way to down-weight foregrounds and yields the smallest

possible error bars on a measurement (Tegmark 1997; Bond et al. 1998). The covariance matrix  $\mathbf{C}$ , which in our case describes covariances between frequency channels, can be estimated in a variety of ways. Given perfect foreground, instrumental, and EoR models, we could form  $\mathbf{C}$  in a way that accurately describes our measured data. However, if our foreground model is flawed for example, our estimate of  $\mathbf{C}$  would not be successful at down-weighting them in the data.

Therefore, one attractive way to estimate  $\mathbf{C}$  is to empirically derive it from the data vector  $\mathbf{x}$  itself:

$$\hat{\mathbf{C}} \equiv \langle \mathbf{x}\mathbf{x}^\dagger \rangle_t, \quad (3)$$

assuming  $\langle \mathbf{x} \rangle = 0$ , where  $\langle \rangle$  denotes a finite average over time  $t$ . The inverse covariance matrix is therefore  $\mathbf{R} = \hat{\mathbf{C}}^{-1}$ .

First, we compute the power spectrum of  $\mathbf{x}$  using OQE formalism and a weighting matrix of  $\hat{\mathbf{C}}^{-1}$ . The result is shown in green in the left plot of Figure 2. Also plotted in the figure are the unweighted ( $\mathbf{R} = \mathbf{I}$ ) power spectrum of  $\mathbf{x}_{FG}$  (blue) and  $\mathbf{x}_{EoR}$  (red).

As shown, our inverse covariance-weighted result successfully suppresses foregrounds. It is also evident that our result fails to recover the EoR signal — it exhibits the correct shape, but the amplitude level is slightly low. This is evidence of signal loss. In order to understand the behavior of this result, we can closely study our covariance matrix,  $\hat{\mathbf{C}}$ , which is shown in Figure 3.

If  $\mathbf{C}$  is computed from the data itself, it carries the risk of over-fitting information in the data and introducing a multiplicative bias to estimates of the signal. For a mathematical derivation of signal loss arising from a data-estimated covariance matrix, see Appendix A. Here we will describe the origin of this signal loss intuitively.

It turns out that because we estimated  $\hat{\mathbf{C}}$  from our data, its eigenspectrum differs from the eigenspectrum of our true  $\mathbf{C}$ , and this difference has consequences on our result. An eigenspectrum ranks the eigenvalues of a matrix from highest to lowest and can be thought of as a spectrum of weights that are given to each spectral mode in the data. In other words, the eigenvalues encode the strength of different shapes in the dataset. The eigenspectrum of the identity matrix  $\mathbf{I}$  is flat (all 1's) because it gives equal weighting to all modes. This is usually not the case for a covariance matrix, in which a sloped eigenspectrum means that modes are given different weights. When weighting data by an inverse covariance matrix, the modes with the highest eigenvalues are down-weighted the most.

If the true covariance matrix  $\mathbf{C}$  of our data was known, then every single eigenvalue of  $\mathbf{C}$  would be representative of real fluctuations in the data. However, when using an estimated  $\hat{\mathbf{C}}$  that is derived from one particular data realization, some of its eigenvalues may be describing random fluctuations that just happen to exist in the data realization. Said differently, shapes that may not exist (or have a weaker existence) in a true



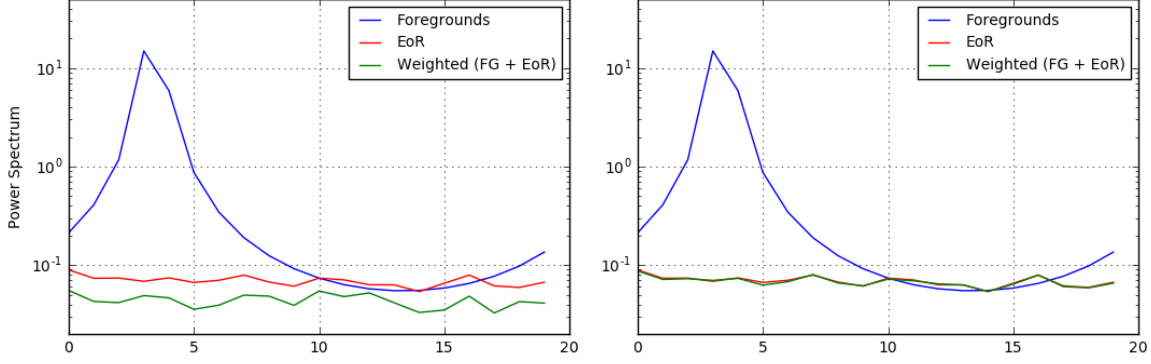


**Figure 2.** Resulting power spectrum estimates for the toy model simulation described in Section 2.1.1 — foregrounds only (blue), EoR only (red), and the weighted FG + EoR dataset (green). We use inverse covariance weighting where  $\hat{\mathbf{C}}$  is derived from the data (left), contrasted with projecting out the first eigenmode only (right). In the former case, signal loss arises from using information from all eigenmodes of  $\hat{\mathbf{C}}$ . Because  $\hat{\mathbf{C}}$  is empirically estimated, its eigenvalues pose the risk of describing random fluctuations that happen to exist in the data realization but may not exist in the true covariance. Consequently, these modes are over-fitted and down-weighted, leading to signal loss. There is no signal loss when using only the zeroth eigenmode, since we are not using information from the weaker eigenmodes which  $\hat{\mathbf{C}}$  does not describe accurately.

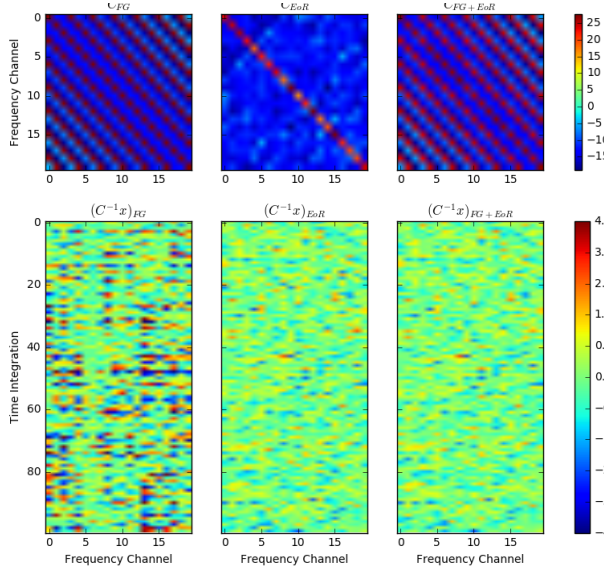


**Figure 3.** The covariance matrices (top row) and inverse covariance-weighted data (bottom row) for FG only (left), EoR only (middle), and FG + EoR (right). Real parts are shown here.

covariance may appear stronger in the estimated covariance. Hence, they will be down-weighted more than they should be.

In general, the strongest modes of  $\hat{\mathbf{C}}$  (highest eigenvalues) are more trustworthy than the weakest modes, since that's where we expect bright foregrounds — the most prominent shapes — to be. If bright foregrounds dominate, these highest eigenvalue modes therefore exist in both  $\mathbf{C}$  and  $\hat{\mathbf{C}}$ . This is demonstrated in the toy model by the successful suppression of the foreground mode, where our estimated covariance matrix identifies the sinusoid and assigns it the highest eigenvalue (the peak in Figure 4).

The danger of an empirically estimated covariance ma-

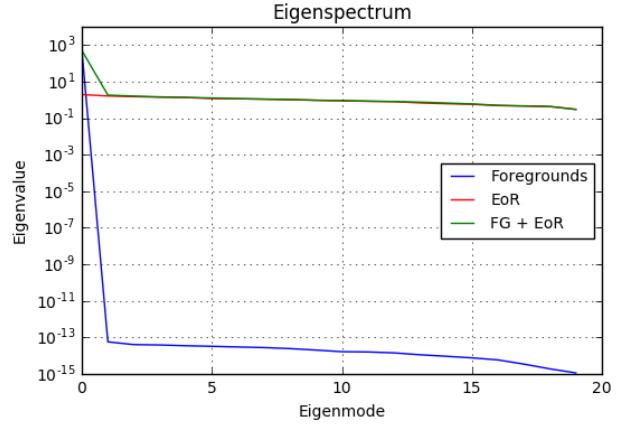


**Figure 4.** Eigenspectrum of  $\hat{\mathbf{C}}_{FG}$  (blue),  $\hat{\mathbf{C}}_{EoR}$  (red), and  $\hat{\mathbf{C}}_{FG+EoR}$  (green). The eigenspectrum of  $\hat{\mathbf{C}}_{FG}$  peaks at the zeroth eigenmode, due to the presence of only one sinusoid. These empirically estimated covariance matrices yield eigenspectra that are different from that of a true  $\mathbf{C}$ , meaning that some eigenmodes (shapes in the data) may be down-weighted more significantly than they should be, producing signal loss.

trix comes from not being able to describe weak eigenmodes of  $\mathbf{C}$  accurately. Instead, the weak eigenmodes of  $\hat{\mathbf{C}}$  may characterize noise-like fluctuations which will be down-weighted. These noise fluctuations could be the signal itself, since  $\hat{\mathbf{C}}$  is constructed using data that contains the signal. This leads to the ‘overfitting’ of noise (or ‘overfitting’ of signal), which is signal loss.

Using what we’ve learned about the eigenspectrum, we can tweak it in a simple way to suppress foregrounds and yield zero signal loss. Namely, we can project out the zeroth eigenmode (i.e. zero out all eigenmodes except the first one), thereby down-weighting the foregrounds perfectly and nothing else. Hence, we are not using information from all the weaker eigenmodes which carry the risk of describing fluctuations that may not

exist in the true covariance. Altering  $\hat{\mathbf{C}}$  as such is one example of a regularization method, in which we are changing  $\hat{\mathbf{C}}$  in a way that flattens its eigenspectrum, making it more similar to that of  $\mathbf{I}$ . The resulting power spectrum estimate for this case is shown in the right plot of Figure 2. In this case we recover EoR, demonstrating that if we can model our foregrounds perfectly (and disentangle them from other modes), we can down-weight them without signal loss. There are several other ways to regularize  $\hat{\mathbf{C}}$ , and we will discuss some in Section 2.1.3.

### 2.1.2. Toy Model: Fringe-Rate Filtering

We have shown how signal loss can arise due to inaccurately characterizing weak eigenmodes with a data-estimated covariance. We will next show how this effect is exaggerated by reducing the total number of independent samples in a dataset.

A fringe-rate filter is an analysis technique designed to maximize sensitivity by integrating in time (Parsons et al. 2016). Rather than a traditional box-car average, a time domain filter can be designed to up-weight temporal modes relevant to things that move as expected for the sidereal motion on the sky, while down-weighting modes which are noise-like.

Because fringe-rate filtering is analogous to averaging in time, it comes at the cost of reducing the total number of independent samples in the data. To mimic this filter, we average every four time integrations of our toy model dataset together, yielding 25 independent samples in time (Figure 5, left). We choose these numbers so that the total number of independent samples is similar to the number of frequency channels — therefore, our matrices will be full rank.

The resulting eigenspectrum as compared to the green curve (FG + EoR) in Figure 4 is shown in Figure 5 (right plot). The spectrum, in the case of fringe-rate filtering (dashed line), falls more steeply, especially for the last few eigenmodes. This is because we have fewer independent modes — **[CC: need help filling out the rest here... and also citing galaxy lit]**.

The power spectrum results for inverse covariance weighted fringe-rate filtered data is shown in Figure 6. As expected, there is a much larger amount of signal loss for this time-averaged dataset. Additionally, because of the steepened eigenspectrum, most of our power spectrum information is coming from only the last few modes and as a result, it is a noisier estimate. This is evident by noticing that the green curve in Figure 6 fails to trace the shape of the unweighted EoR power spectrum.

Using our toy model, we have seen that a sensitivity-driven analysis technique like fringe-rate filtering has trade-offs of signal loss and noisier estimates when using data-estimated covariance matrices. Longer integrations increase sensitivity but reduce the number of independent samples, resulting in weakly characterized, steep eigenspectra that can overfit noise greatly. **[CC: help me fix explanation]**

### 2.1.3. Toy Model: Other Weighting Options

In Section 2.1.1 we showed one example (projecting the zeroth eigenmode) of how altering  $\hat{\mathbf{C}}$  can make the difference between zero and some signal loss, if we can distinguish between real eigenmodes in a true covariance matrix from random fluctuation-induced eigenmodes in an estimated one. We will now use our toy model to describe several other ways to tailor  $\hat{\mathbf{C}}$  in order to minimize signal loss. We illustrate the resulting power spectra and eigenspectra for four different cases in Figures 7 and 8.

As a first test, we know that our simulated EoR should have a covariance matrix that mimics the identity matrix, with its variance encoded along the diagonal. If we model  $\mathbf{C}_{EoR}$  as such, instead of computing it based on the dataset itself, and add it to  $\hat{\mathbf{C}}_{FG}$  (defined as  $\hat{\mathbf{C}}_{FG} = \langle \mathbf{x}_{FG} \mathbf{x}_{FG}^\dagger \rangle$ ) to obtain a final  $\hat{\mathbf{C}}$  to use in weighting, we see that there is negligible signal loss (Figure 7, upper left). This is because by modeling  $\mathbf{C}_{EoR}$ , we avoid over-fitting small fluctuations in the data that our model doesn't know about (but an empirically derived  $\hat{\mathbf{C}}$  would). This is evident when comparing the green and red curves in Figure 8. We don't see perfect EoR recovery though, as the green and red curves differ at one  $k$  value in Figure 7. This deviation is a consequence of the difference between the true and modeled covariance matrices.

The second panel (top right) in Figure 7 uses a regularization method of setting  $\hat{\mathbf{C}} = \hat{\mathbf{C}}_{ij} + \gamma \mathbf{I}_{ij}$ , where  $i=j=20$  (number of frequencies) and  $\gamma = 5$  (an arbitrary strength of  $\mathbf{I}$  for the purpose of this toy model). By adding the identity matrix, element-wise, we are weighting the diagonal elements of the matrix more heavily than those off-diagonal, thereby flattening out its eigenspectrum. If all modes are given similar weights, we avoid down-weighting artificial modes more than others.

The third panel (bottom left) in Figure 7 flattens out the eigenspectrum of  $\hat{\mathbf{C}}$  a different way - by only using the first three eigenmodes. This means that all but the three highest weights will be replaced with 1's (equal weights). Again, flattening the eigenspectrum results in negligible signal loss. However, we do not perfectly recover the shape of EoR because we lost information when projecting out certain modes.

The last regularization scheme we are highlighting here is setting  $\hat{\mathbf{C}} = \hat{\mathbf{C}}_{ij} \mathbf{I}_{ij}$ , or inverse variance weighting (keeping only the diagonal elements of  $\hat{\mathbf{C}}$ ). In the bottom right panel of Figure 7, we see that this method does a poor job down-weighting foregrounds. For this toy model, our foregrounds are spread out in frequency and therefore have non-negligible frequency-frequency correlations. Multiplying by the identity, element-wise, results in a diagonal matrix, meaning we are only left with correlation information between the same two frequencies. Because we disregard information from all other frequency combinations in this case, we do a poor job suppressing the foreground. But because we flattened the eigenspectrum, we also avoid signal loss.

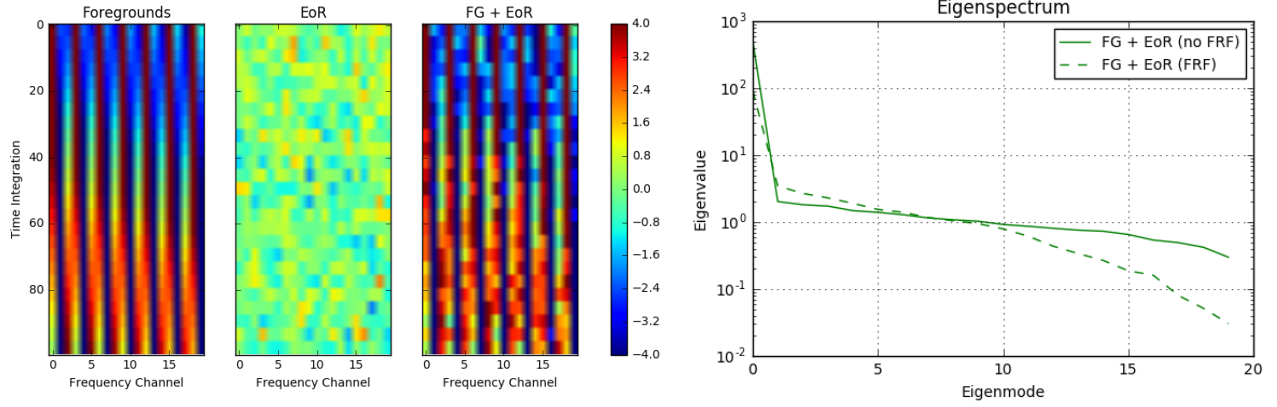


**Figure 5.** Left: Our ‘fringe-rate filtered’ (time-averaged) toy model dataset. We average every four samples together, yielding 25 independent samples in time. Real parts are shown here. Right: Eigenspectrum of  $\hat{\mathbf{C}}_{FG+EoR}$ , in the case of no fringe-rate filtering (solid green) and with fringe-rate filtering (dashed green). The dashed spectrum is steeper, resulting in more dramatic differences in weighting between eigenmodes. Consequently, if all eigenmodes are used in weighting it is possible to down-weight random noisy modes more severely than for the non-averaged case.

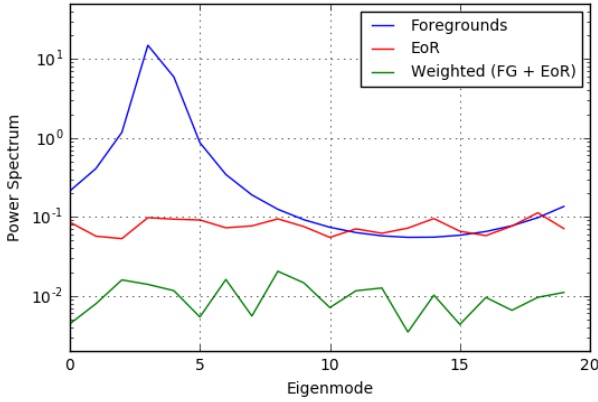


**Figure 6.** Resulting power spectrum estimate for the fringe-rate filtered toy model simulation — foregrounds only (blue), EoR only (red), and the weighted FG + EoR dataset (green). We use inverse covariance weighting where  $\mathbf{C}$  is derived from the data. There is a larger amount of signal loss than for the non-averaged data, a consequence of a steepened, weakly characterized eigenspectrum from using fewer independent modes in the data. The power spectrum estimate is also noisier, since most of the information used in constructing the estimate came from only a few eigenmodes.

Although the fourth method did not successfully recover EoR for this particular simulation, it is important that we show that there are many options for estimating a covariance matrix, and some may be more effective than others based on the spectral nature of the components in a dataset. One may imagine a situation where a particular systematic is contained to an isolated frequency (such as radio frequency interference or crosstalk). In such a case, preserving only the diagonal elements of  $\hat{\mathbf{C}}$  would be an effective way of removing this contamination.

In summary, we have a choice of how to weight 21 cm data. Ideally, we want to down-weight bright foregrounds without removing the underlying cosmological signal. As we investigated however, there are trade-offs between the weighting method used, its foreground-

removal effectiveness, and the amount of resulting signal loss.

## 2.2. Error Estimation

Our second major 21 cm power spectrum theme is error estimation, as we desire robust methods for determining accurate confidence intervals for our measurements. Two popular ways of estimating errors on a power spectrum measurement are calculating the variance of a dataset, and computing a theoretical error estimate based on an instrument’s system temperature and observational parameters. In a perfect world, both methods would match up. However, in practice the two don’t always agree due to a number of factors, including time, frequency, and antenna-dependent noise and non-uniform weightings. Since modeling errors for a complex instrument is only approximate, we choose to compute error bars on our measurements that have been derived from its inherent variance.

A common technique used to estimate the error in a measurement is bootstrapping. Bootstrapping uses sampling with replacement to estimate a posterior distribution. For example, power-spectral measurements of 21 cm data can be made along many axes, including time and baselines. Averaging each sample set gives us a realization of the power spectrum answer. Realizations are correlated with each other to a degree set by the fraction of sampled points that are held in common between them. Hence, through the process of resampling and averaging along these axes, we can estimate error bars for our results which represent the underlying distribution of power spectra values that are allowed by our measurements.

Again, we focus on toy models to highlight traps that one can fall into when bootstrapping power spectra. Suppose we have a Gaussian random signal dataset of length  $N = 1000$  and unity variance. We are interested in the average of the dataset, and predict that the error on the mean should obey  $1/\sqrt{N}$ , where  $N$  is the number

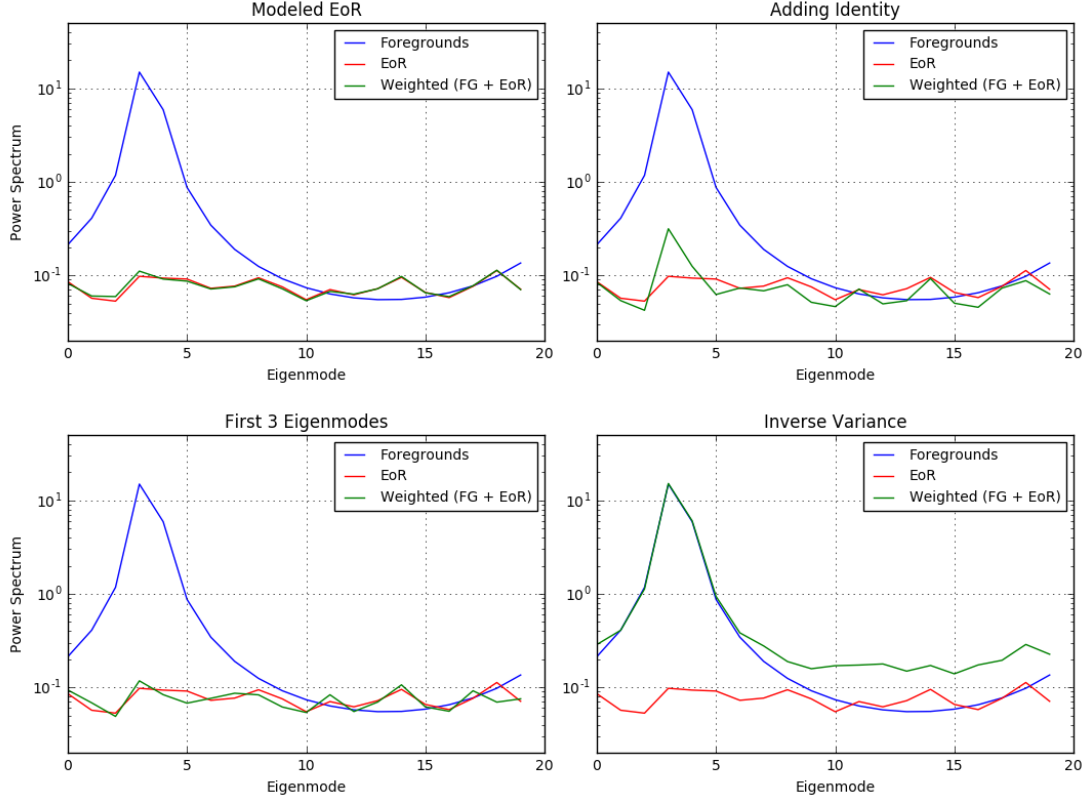


**Figure 7.** Resulting power spectra estimates for our fringe-rate filtered toy model simulation — foregrounds only (blue), EoR only (red), and the weighted FG + EoR dataset (green). We show four alternate weighting options that each avoid signal loss, including modeling the covariance matrix of EoR (upper left), regularizing  $\hat{\mathbf{C}}$  by adding an identity matrix to it (upper right), using only the first three eigenmodes of  $\hat{\mathbf{C}}$  (lower left), and keeping only the diagonal elements of  $\hat{\mathbf{C}}$  (lower right).

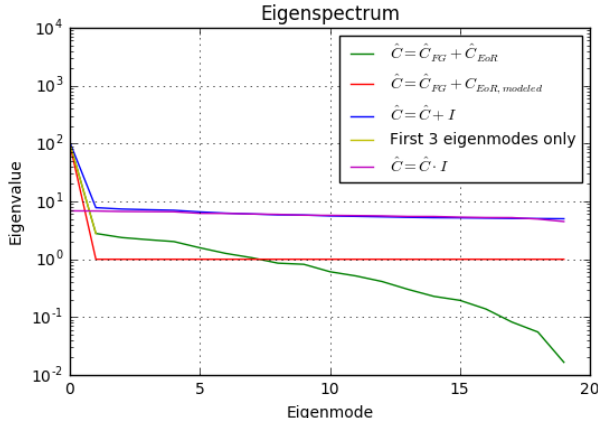


**Figure 8.** We compare the eigenspectrum of an empirically calculated  $\hat{\mathbf{C}}$  (green) to that of four alternate weighting options, including modeling the covariance matrix of EoR (red), regularizing  $\hat{\mathbf{C}}$  by adding an identity matrix to it (blue), using only the first three eigenmodes of  $\hat{\mathbf{C}}$  (yellow), and multiplying an identity matrix with  $\mathbf{C}$  (magenta).

of samples.

We form 100 bootstraps, each comprised of an array of length  $N$  that is created by a random resampling of the original data, with replacement. The standard deviation over the 100 bootstraps gives an error estimate for our

dataset. As shown in Figure 9 by the grey star, the error computed from bootstrapping matches our theoretical prediction.

One major caveat of bootstrapping arises when working with correlated data. If, for example, a dataset has many repeated values inside it, this would be reflected in each bootstrap. The same value would be present multiple times within a bootstrap and also be present between bootstraps, purely because it has a more likely chance of being drawn if there are repeats of itself. Therefore, bootstrapping correlated data results in a smaller variation between bootstraps, and hence, under-estimates errors. The use of a fringe-rate filter, which averages data in time to increase sensitivity, is one example which leads to a reduction in the number of independent samples, creating a situation in which errors can be under-estimated. We will now show this effect using our toy model.

Going back to our toy model, we apply a sliding boxcar average to 10 samples at a time, thus reducing the number of independent samples to  $N/10 = 100$ . Bootstrapping this time-averaged noise, using the same method as described earlier (drawing  $N = 1000$  samples), under-estimates the error by a factor of  $\sim 3$ . This occurs because we are drawing more samples than independent ones available, and thus some samples are repeated mul-



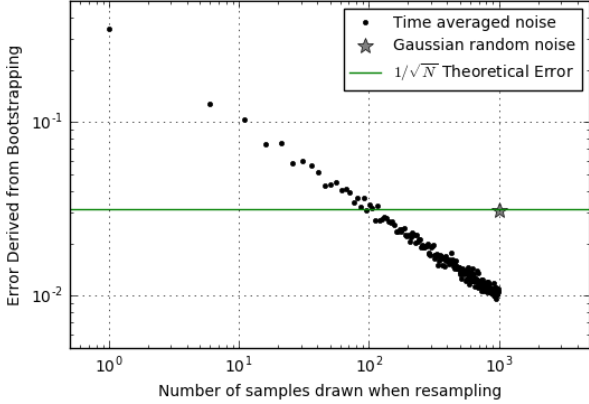


**Figure 9.** Error estimation produced by bootstrapping as a function of the number of samples drawn when sampling with replacement. The star represents the error associated with drawing 1000 samples from a length 1000 array of a Gaussian random signal. The black points correspond to time-averaged data (correlated data) which has 100 independent samples. They illustrate how errors can be underestimated if drawing more samples than there are independent samples in the data. The estimated errors match up with the theoretical prediction only at  $N = 100$ .

multiple times in all bootstraps, leading to less variation between the bootstraps. In fact, the error derived from bootstrapping is a strong function of the number of samples that are drawn (Figure 9, black points), and we can both under-estimate the error by drawing too many or over-estimate it by drawing too few. However, if we know that we have 100 independent samples, the error associated with drawing 100 samples with replacement does match the theoretical prediction as expected.

This example highlights the importance of understanding how analysis techniques (e.g. fringe-rate filtering) can affect a common statistical procedure like bootstrapping. Bootstrapping as a means of estimating power spectrum errors from real fringe-rate filtered data requires knowledge of the number of independent samples, which is not always a trivial task. For example, computing the effective number of independent samples of fringe-rate filtered data is not as simple as counting the number of averages performed. Down-sampling a fringe-rate filtered signal is straightforward using a boxcar average, but non-trivial with a more complicated convolution function that has long tails. Hence, we do not recommend bootstrapping unless the number of independent samples along the axis that is being re-sampled is well-determined.

We will now discuss a second subtle feature of bootstrapping that can lead to an over-estimation of errors. Suppose we have 5 independent measurements of the sky (from 5 different baselines, for example). A bootstrap then consists of 5 measurements that are drawn randomly with replacement from the original set. If all 5 spaces are filled randomly, there is a high probability that some measurements will be repeated in the bootstrap because they are drawn more than once. The bootstrap may therefore consist of only 3 or 4 indepen-

dent measurements — a number smaller than the total number of samples. In fact, the probability of drawing 5 completely independent measurements is less than 4%.

In order to maximize sensitivity, we desire as many independent samples as possible. However, solely using all 5 independent measurements does not allow variation between bootstraps.

Therefore, we use a slightly modified bootstrapping method. For each bootstrap, we draw  $N - 1 = 4$  samples without replacement and draw the last slot randomly with replacement. In doing so there is a small chance a bootstrap will consist of 5 independent samples, but even with 4 our sensitivity is nearly maximized. One may wonder whether this change is still a legitimate way of error estimating since random sampling only occurs for one value in a bootstrap. However, as long as the number of possible variations is greater than the number of bootstraps we perform, it is a valid way to uncover the inherent variability in a dataset.

In Figure 10 we compare the two methods of bootstrapping: sampling all elements randomly (black points) versus sampling just the final element randomly (grey points). The two converge for datasets with small numbers of elements, when filling a few spots randomly is nearly the same as filling only the last spot randomly. However, there is also increased scatter in this regime due to small number statistics.

The difference between the two methods is most pronounced for datasets with large numbers of elements. As a dataset grows in size, it becomes increasingly rare to draw entirely independent samples, and thus the benefit of ensuring, say, 999 independent samples out of 1000 is most noticeable. The more elements in our dataset, the more sensitivity we can gain by mandating that most of our measurements are independent ones. An analog for the y-axis in Figure 10 is therefore the sensitivity of a final power spectrum measurement.

In summary, bootstrapping can be an effective and straightforward way to estimate errors of a dataset. However, we have illustrated two situations in which bootstrapping can lead to under-estimated errors and sensitivities. First, we have shown that bootstrapped error depends strongly on the number of elements drawn in a bootstrap sample. Estimated errors can drop to arbitrarily small values when the number of elements drawn exceeds the effective number of independent elements. We have also shown a situation in which a bootstrapping method does not provide the most sensitive measurement possible. While bootstrapping is convenient because it provides a way to estimate errors from the data itself, one must assess whether certain analysis choices have compromised the method and whether a variation of traditional re-sampling could be preferred instead.

### 2.3. Bias

In a 21 cm power spectrum, detections could be the EoR signal, but they could also (and unfortunately more

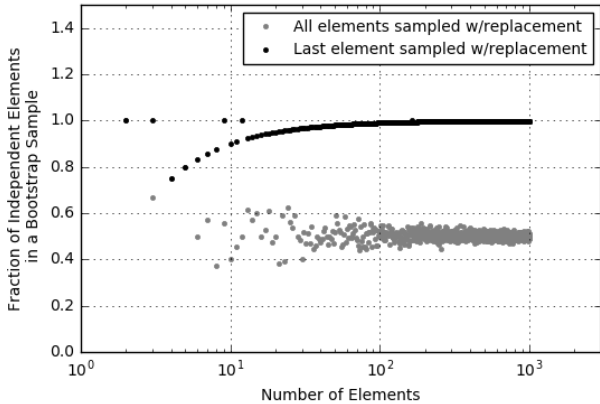


**Figure 10.** The fraction of independent elements in one bootstrap sample as a function of the total number of elements in a dataset (i.e. 4 out of 5 elements are independent would yield a fraction of 0.8). A fraction of 1.0 means that all elements in the bootstrap sample are independent, and therefore sensitivity is maximized (alternately, this axis can be thought of as power spectrum sensitivity, where sensitivity increases moving upwards along the y-axis). Two bootstrapping methods are shown here — sampling all elements with replacement (grey) and sampling only the last element with replacement (black). The former fails to maximize sensitivity since some elements end up being repeated due to random sampling. The ‘outlier’ points lying at a fraction of 1.0 occur in the off-chance that the last spot in the sample happens to be the one missing element instead of a repeated element — this is more likely to happen with a small total number of elements but also results in a more dramatically different fraction as compared to the case of a repeated element in the last spot, hence why these points appear like outliers.

likely) be attributed to other sources of bias. Connecting a detection to EoR as opposed to noise or foreground bias is a key challenge of future 21 cm data analyses. In this section we will discuss possible sources of bias in a measurement, as well as techniques that can help mitigate their effects. We will also present a series of tests which we suggest be used to help evaluate deep limits and/or detections.

### 2.3.1. Foreground and Noise Bias

Foreground bias is perhaps one of the main factors limiting 21 cm results. Foreground signals lie  $\sim 4$ -5 orders of magnitude above the cosmological signal. Though there are many techniques proposed for removing foregrounds, most experiments remain ultimately limited by residuals rather than noise.

Because foreground spectra are smooth in frequency, they preferentially show up at low delay, or  $k$  modes. For a particular baseline length, there is a maximum delay imposed on foregrounds, which corresponds to the light-crossing time between the two antennas in the baseline. For longer baselines, this value increases, producing what is known as “the wedge” (Parsons et al. 2012; Liu et al. 2014a; Liu et al. 2014b; Vedantham et al. 2012; Thyagarajan et al. 2013; Pober et al. 2013; Datta et al. 2010). The wedge describes a region in  $k$ -space contaminated by foregrounds, bounded by baseline length (which is proportional to  $k_{\perp}$ ) and delay (which is pro-

portional to  $k_{\parallel}$ ). Properties of the wedge can be used to isolate and remove foregrounds, as done by Ali et al. (2015), Parsons et al. (2014), and Jacobs et al. (2015).

However, this isolation is not perfect. In deep measurements, power spectrum measurements at  $k_{\parallel}$  values beyond the length of a baseline are often still contaminated at a low level. This leakage can be attributed to convolution kernels associated with Fourier-transforming visibilities into delay-space. In other words, smooth-spectrum foregrounds appear as  $\delta$ -functions in delay-space, convolved by the Fourier transform of the source spectrum and the antenna response, both of which could smear out the foregrounds and cause leakage outside the wedge.

There are analysis techniques to mitigate the effects of foreground leakage and prevent information from low  $k$ ’s from spreading to high  $k$  values. For example, narrow window functions can be used to minimize the covariance of a particular  $k$  value with other ones (Liu et al. 2014b). In other words, one can construct an estimator using OQE that forces a window function to have a minimum response to low  $k$  values. The window function used in Ali et al. (2015) is constructed in such a way, specifically to prevent foregrounds that live at low  $k$ ’s from contaminating higher  $k$ -modes (see Section 3.3). Minimizing foreground leakage in this way however, comes with the trade-off of compromising power spectrum sensitivity, since narrow window functions increases errors for each  $k$ -mode (Liu et al. 2014b).

Confirming foreground detections at higher  $k$ ’s is more difficult. In the next section, we will present some tests that can help distinguish these excesses from that of EoR.

In addition to foreground bias, noise can also be responsible for positive power spectrum detections if thermal noise is multiplied by itself. Every 21 cm visibility measurement contains thermal noise that is comprised of receiver and sky noise. We expect this noise to be independent between antennas and thus we can beat it down (increase sensitivity) by integrating longer, using more baselines, etc. However, the squaring of noise occurs when cross-multiplying visibilities, which is shown by the two copies of  $\mathbf{x}$  in Equation (1). If both copies of  $\mathbf{x}$  come from the same baseline and time, it can result in power spectrum measurements that are higher than those predicted by the thermal noise of the instrument. One way to avoid this type of noise bias is to avoid cross-multiplying data from the same baselines or days. This ensures that the two quantities that go into a measurement have separate noises that don’t correlate with each other.

Another type of noise bias can stem from the spurious cross-coupling of signals between antennas. This excess is known as instrumental crosstalk and is an inadvertent correlation between two independent measurements via a coupled signal path. Crosstalk appears as a constant phase bias in time in visibilities, and it varies slowly compared to the typical fringe-rates of sources. Because it

is slow-varying, crosstalk can be suppressed using time-averages or fringe-rate filters. However, there remains a possibility that power spectrum detections are caused by residual, low-level crosstalk which survived any suppression techniques.

In the next section, we approach the difficult task of tracing excesses to foreground, noise, and EoR biases through a discussion of useful jackknife tests.

### 2.3.2. Jackknife Tests

The jackknife is a resampling technique in which a statistic (i.e. power spectrum) is computed in subsets of the data. These subsets are then compared to reveal systematics. In this section we define two main tests — the null test and the traditional jackknife — and explain how a power spectrum detection must pass each. We then highlight how these tests can be used to help distinguish between different sources of bias.

- **Null Test:** A null test is a type of jackknife test that removes the astronomical signal from data in order to investigate underlying systematics. Several null tests on data are described in [Keating et al. \(2016\)](#). For example, one can divide data into two subsets by separating odd and even julian dates, or the first half of the observing season from the second. Subtracting the two removes signal that is common to both subsets, including foregrounds and EoR. The resulting power spectrum should be consistent with thermal noise estimates; if it is not, it suggests the presence of a systematic that differs from one of the data subsets to the other (i.e. doesn't get subtracted perfectly).
- **Traditional Jackknife:** In a more broad sense, it is important to perform many jackknife tests in order to instill confidence in a final result, since a stable result should be consistent through all of them. A result must be steadfast throughout all jackknives no matter how the data is sliced. Jackknives can be taken along several different axes — for example, one could start with a full dataset, and compute a power spectrum each time as a day of data is removed, or a baseline is removed. This type of jackknife would reveal bias present only at certain LSTs (such as a foreground source), for example, or misbehaving baselines.

While the null test hunts for deviations from thermal noise and the jackknife tests for deviations in subsamples, they are both closely related. We can highlight the connection between the two using a toy model dataset.

Suppose we have two measurements (for example, from two baselines),  $\mathbf{x}_a$  and  $\mathbf{x}_b$ . The measurements have dimensions of 200 time integrations and 20 frequency channels. They each have separate thermal noises constructed as a Gaussian random signal for each, and identical EoR signals.

To mimic the presence of a systematic in part of the measurement, we add a toy sinusoid foreground, similar

to the one used in Section 2.1.1, to the first 100 time integrations of both measurements. This represents a foreground signal present in, for example, the first half of the LST range used for analysis, but not the second half. Mathematically, if  $\mathbf{n}$  is noise,  $\mathbf{e}$  is the EoR signal, and  $\mathbf{fg}$  is the foreground signal, the two measurements (which are cross-multiplied to form power spectra) can be written as:

$$\mathbf{x}_a = \mathbf{n}_a + \mathbf{e} + \mathbf{fg} \quad (4)$$

$$\mathbf{x}_b = \mathbf{n}_b + \mathbf{e} + \mathbf{fg}, \quad (5)$$

where the two jackknife samples (for both  $a$  and  $b$ ) are:

$$\mathbf{x}_1 = \mathbf{n} + \mathbf{e} + \mathbf{fg} \quad (6)$$

$$\mathbf{x}_2 = \mathbf{n} + \mathbf{e} \quad (7)$$

For example,  $\mathbf{x}_{1a}$  represents a jackknife sample (first half of the data) for the first measurement. Similarly,  $\mathbf{x}_{2b}$  represents a jackknife sample (second half of the data) for the second measurement.

We do not perform a time-average or apply a fringe-rate filter to this toy model, since we are interested only in what jackknife tests can tell us about biases. For the same reason, we use a weighting matrix of  $\mathbf{I}$  for power spectrum estimation to avoid signal loss.

We form 3 different power spectrum estimates shown in Figure 11. The first is a null test where we subtract  $\mathbf{x}_2$  from  $\mathbf{x}_1$  for both measurements  $a$  and  $b$ . This is equivalent to splitting up a full dataset along an axis (in this case, time) and subtracting the two to remove sky signal that should ideally be present in both. We cross-multiply measurements  $a$  and  $b$  to form an un-biased (noise-wise) estimate (blue curve). The second estimate, shown in red, is the same null test with the foreground systematic removed (eliminate  $\mathbf{fg}$  in Equations 4 and 5). Finally, we also show the noise power spectrum (green).

From this test we see a clear difference between the null test with the presence of the foregrounds, and the power spectrum of noise. This signifies a non-EoR bias that is only present in either  $\mathbf{x}_1$  or  $\mathbf{x}_2$ .

While the null test is useful for testing noise properties and the uniformity of a dataset, jackknives are useful in pinpointing which data subsets are contaminated by biases and which are not; in our toy model we see that the bias exists only in  $\mathbf{x}_1$  (Figure 12). If foreground or noise biases exist in a dataset, jackknives can tease them out and provide insight into possible sources. For example, if jackknives along the time-axis reveal a bias present at a certain LST, a likely explanation would be excess foreground emission from a radio source in the sky at that time. A jackknife test involving data before and after the application of a fringe-rate filter can reveal whether cross-talk noise bias is successfully suppressed with the filter, or if similar-shaped detections in both power spectra suggest otherwise. There are many other jackknife axes of which we will not go into detail here, including baseline, frequency, and polarization. Ultimately,

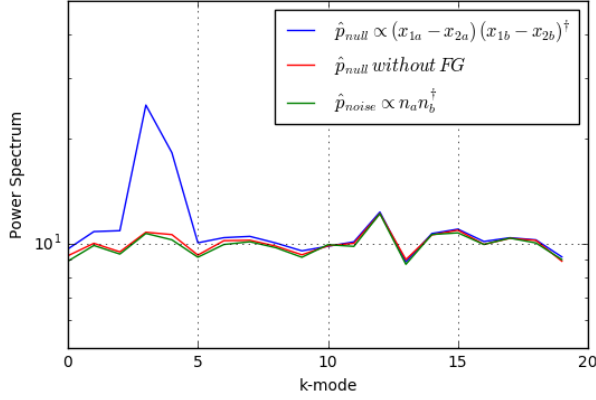


**Figure 11.** Power spectrum estimates for a null jackknife test with the presence of a foreground systematic (blue), without the foreground systematic (red), and noise alone (green). Because the first null test is not consistent with noise, it suggests the presence of a systematic in either  $\mathbf{x}_1$  or  $\mathbf{x}_2$ . Null tests of clean measurements should be consistent with thermal noise.

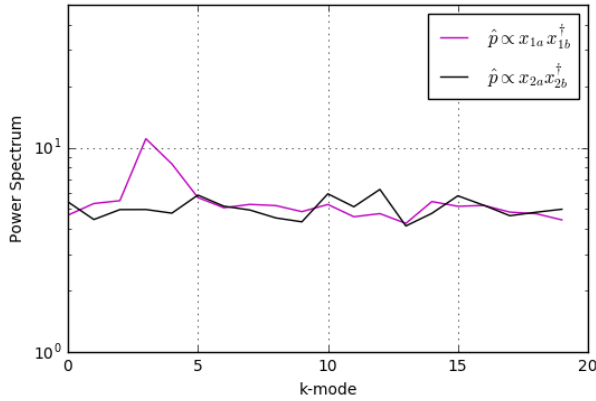


**Figure 12.** Power spectrum estimates for  $\mathbf{x}_1$  and  $\mathbf{x}_2$ , two jackknives of the toy model. They suggest the presence of a systematic in  $\mathbf{x}_1$  only, illustrating how jackknives can be used to tease out excesses. Clean measurements should remain consistent despite the jackknife taken.

an EoR detection should persist through them all and a clean measurement should exhibit noise-like null spectra.

In this section we have highlighted how null tests and jackknife tests are key for determining the nature of a power spectrum detection. In Section 3.3 we perform some examples of these tests on PAPER-64 data in order to prove that our excesses are not EoR and to identify their likely cause.

### 3. DEMONSTRATION IN PAPER-64 DATA

In the previous sections we have discussed three overarching 21 cm power spectrum themes — signal loss, error estimation, and bias. Understanding the subtleties and trade-offs involved in each is necessary for an accurate and robust understanding of a power spectrum result.

We now present a case study of these same three

themes using data from the PAPER experiment. We use the intuition developed through the toy model simulations in order to make a new analysis of the PAPER-64 dataset originally presented in Ali et al. (2015) and obtain a revised power spectrum estimate.

As a brief review, PAPER is a dedicated 21 cm experiment located in the Karoo Desert in South Africa. The PAPER-64 configuration consists of 64 dual-polarization drift-scan elements that are arranged in a grid layout. For our case study, we focus solely on Stokes I data from PAPER’s 30 m East/West baselines. For information about the backend system of PAPER-64, its observations, and data reduction pipeline, we refer the reader to Parsons et al. (2010) and Ali et al. (2015).

The previously best published 21 cm upper limit result from Ali et al. (2015) uses 124 nights of data to place a  $2\sigma$  upper limit on  $\Delta^2(k)$ , defined as

$$\Delta^2(k) = \frac{k^3}{2\pi^2} \hat{p}(k), \quad (8)$$

of  $(22.4 \text{ mK})^2$  in the range  $0.15 < k < 0.5 \text{ h Mpc}^{-1}$  at  $z = 8.4$ .

For our analysis, we use 8 hours of LST (RA 0.5-8.6 hours) and 51 total baselines (Ali et al. (2015) uses an RA range of 0-8.6 hours). All power spectrum results are produced for a center frequency of 151 MHz using a width of 10 MHz (20 channels), identical to the analysis in Ali et al. (2015). We note that the PAPER-64 dataset that we use in this case study differs from that in Ali et al. (2015) mainly by the fringe-rate filter. [CC: Danny says the next part is wrong... ] In Ali et al. (2015), the applied filter was degraded by widening it in fringe-rate space. This was chosen in order to increase the number of independent modes and reduce signal loss. With the development of a robust method for assessing signal loss, we feel comfortable using a narrow filter — the optimal fringe-rate filter — in order to maximize sensitivity. This filter is computed for a fiducial 30 m baseline at 150 MHz, the center frequency in our band. The filter in both the fringe-rate domain and time domain is shown in Figure 13.

#### 3.1. PAPER-64: Signal Loss

In Section 2.1, we showed how signal loss arises when weighting data using information from the data itself. Here we describe a methodology that simulates the injection and recovery of a cosmological signal in order to quantify the amount of signal loss accompanying a weighting scheme. In particular, we highlight major differences from the signal loss computation used in Ali et al. (2015), which previously underestimated losses.

##### 3.1.1. Signal Loss Methodology

To capture the full statistical likelihood of signal loss, one requires a quick way to generate many realizations of simulated 21 cm signal visibilities. Here we use the same method used in Ali et al. (2015), where gaussian noise visibilities are filtered in fringe-rate space to retain



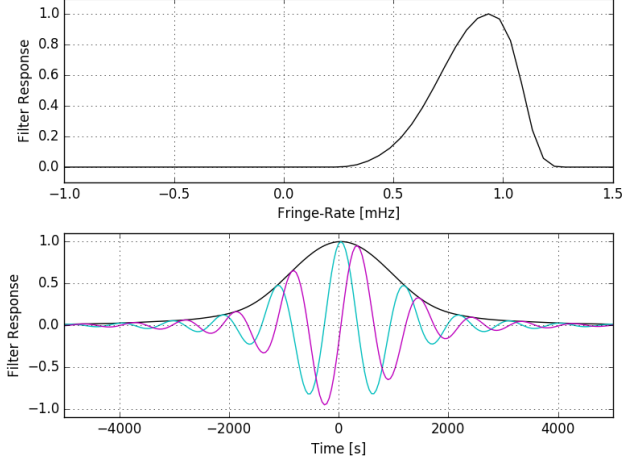


**Figure 13.** Top: the normalized optimal power-spectrum sensitivity weighting in fringe-rate space for our fiducial baseline and Stokes I polarization beam. Bottom: the time-domain convolution kernel corresponding to the top panel. Real and imaginary components are illustrated in cyan and magenta, respectively, with the absolute amplitude in black. The fringe-rate filter acts as an integration in time, increasing sensitivity but reducing the number of independent samples in the dataset.

only “sky-like” time-modes. This signal is then added to the data.<sup>1</sup>

Suppose that  $\mathbf{e}$  is the injected EoR (at some amplitude level), and  $\mathbf{x}$  is our data vector. We define  $\mathbf{r}$  to be the data plus the EoR signal:

$$\mathbf{r} = \mathbf{x} + \mathbf{e}. \quad (9)$$

We are interested in quantifying how much  $\mathbf{e}$  is lost after weighting  $\mathbf{r}$  and applying OQE formalism. We investigate this by comparing two quantities we define as the input power spectrum and output power spectrum:  $P_{in}$  and  $P_{out}$ .  $P_{in}$  represents the unweighted power spectrum of only  $\mathbf{e}$ , our simulated EoR signal.  $P_{out}$  is the weighted power spectrum of  $\mathbf{e}$  that would result from our pipeline if the signal was mixed with our data. Comparing the two quantities yields insight into how much of  $\mathbf{e}$  is lost due to our choice of weighting. Ignoring normalization factors, these two quantities can be written as:

$$P_{in,\alpha} \propto \mathbf{e}^\dagger \mathbf{I} \mathbf{Q}^\alpha \mathbf{I} \mathbf{e} \quad (10)$$

and

<sup>1</sup> One specific change from Ali et al. (2015) is that we add this simulated signal into the chain before the final fringe-rate filter is applied to the data. Previously, the addition was done after that final fringe-rate filter step. This change results in an increased estimate of signal loss, likely due to the use of the fringe-rate filter as a simulator. Whether the loss would be estimated at the same level if different 21 cm simulations were used remains an open question.

$$P_{out,\alpha} \equiv \hat{\mathbf{p}}_{e,\alpha} = \hat{\mathbf{p}}_{r,\alpha} - \hat{\mathbf{p}}_{x,\alpha} \\ \propto \mathbf{r}^\dagger \mathbf{R}_r \mathbf{Q}^\alpha \mathbf{R}_r \mathbf{r} - \mathbf{x}^\dagger \mathbf{R}_x \mathbf{Q}^\alpha \mathbf{R}_x \mathbf{x}. \quad (11)$$

It is noted that the output power spectrum is comprised of two terms: the weighted power spectrum associated with  $\mathbf{r}$ , and that of data  $\mathbf{x}$  alone.

One may wonder why  $P_{out}$  cannot be computed simply as the weighted power spectrum of  $\mathbf{e}$  alone, namely  $P_{out,\alpha} \propto \mathbf{e}^\dagger \mathbf{R}_r \mathbf{Q}^\alpha \mathbf{R}_r \mathbf{e}$ . Expanding Equation (11), we see that  $P_{out}$  is comprised of multiple terms:

$$P_{out,\alpha} \propto (\mathbf{x} + \mathbf{e})^\dagger \mathbf{R}_r \mathbf{Q}^\alpha \mathbf{R}_r (\mathbf{x} + \mathbf{e}) - \mathbf{x}^\dagger \mathbf{R}_x \mathbf{Q}^\alpha \mathbf{R}_x \mathbf{x} \\ \propto \mathbf{x}^\dagger \mathbf{R}_r \mathbf{Q}^\alpha \mathbf{R}_r \mathbf{x} + \mathbf{e}^\dagger \mathbf{R}_r \mathbf{Q}^\alpha \mathbf{R}_r \mathbf{e} + \mathbf{x}^\dagger \mathbf{R}_r \mathbf{Q}^\alpha \mathbf{R}_r \mathbf{e} \\ + \mathbf{e}^\dagger \mathbf{R}_r \mathbf{Q}^\alpha \mathbf{R}_r \mathbf{x} - \mathbf{x}^\dagger \mathbf{R}_x \mathbf{Q}^\alpha \mathbf{R}_x \mathbf{x}. \quad (12)$$

Taking the case of very large  $\mathbf{e}$  so that any terms involving only  $\mathbf{x}$  are small, yields:

$$P_{out,\alpha,e \gg x} \propto \mathbf{e}^\dagger \mathbf{R}_r \mathbf{Q}^\alpha \mathbf{R}_r \mathbf{e} + \mathbf{x}^\dagger \mathbf{R}_r \mathbf{Q}^\alpha \mathbf{R}_r \mathbf{e} \\ + \mathbf{e}^\dagger \mathbf{R}_r \mathbf{Q}^\alpha \mathbf{R}_r \mathbf{x}. \quad (13)$$

We see that our naive expression for  $P_{out}$  is the first term in Equation (13), but there are also two additional terms. An initial assumption would be that the cross-terms that involve both  $\mathbf{e}$  and  $\mathbf{x}$  should be zero, since foregrounds and the cosmological signal are physically unrelated. In Ali et al. (2015), this assumption is used, and the first term in Equation (13) is directly compared to the input (unweighted) power spectrum to compute signal loss.

However, deeper investigations of these terms reveal that they contain non-negligible power. In fact, foreground modes and signal modes are anti-correlated on average, as derived and explained in Switzer et al. (2015). The spurious correlation of the two means that we cannot compute signal loss using a signal-only simulation, which would yield greater values for  $P_{out}$  and thereby underestimate signal loss. Therefore, in our revised signal loss computation we use the full quantity for  $P_{out}$  as defined in Equation (11), which subtracts the weighted power spectrum of the data from the weighted power spectrum of data plus EoR.

The relationship between the input and output power spectra,  $P_{in}$  and  $P_{out}$ , can be thought of as a transfer function which, for a sampling of  $P_{in}$  and  $P_{out}$  provides a mapping from an output power spectrum distribution into an input distribution. By viewing data through this signal loss lens, we are asking the question “what input power spectrum distribution could this (signal-loss affected) data come from?” In the next section, we describe our signal loss transfer function for PAPER-64 data and detail the computation used to translate our power spectrum result into one viewed through a signal loss lens.

### 3.1.2. Signal Loss in Practice

We now shift our attention towards computing signal loss for the fringe-rate filtered PAPER-64 dataset. While our methodology outlined below is robust to any weighting scheme, here we demonstrate the computation using inverse covariance weighting ( $\mathbf{R} = \mathbf{C}^{-1}$ ), the weighting scheme used in Ali et al. (2015) which leads to substantial loss. With this weighting, our expressions for  $P_{in}$  and  $P_{out}$  become:

$$P_{in,\alpha} \propto \mathbf{e}^\dagger \mathbf{I} \mathbf{Q}^\alpha \mathbf{I} \mathbf{e} \quad (14)$$

$$P_{out,\alpha} \propto \mathbf{r}^\dagger \mathbf{C}_r^{-1} \mathbf{Q}^\alpha \mathbf{C}_r^{-1} \mathbf{r} - \mathbf{x}^\dagger \mathbf{C}_x^{-1} \mathbf{Q}^\alpha \mathbf{C}_x^{-1} \mathbf{x} \quad (15)$$

Our signal loss transfer function for one  $k$  value is shown in Figure 14 and compares the weighted case ( $\mathbf{R} = \mathbf{C}^{-1}$ , left plot) with an unweighted case ( $\mathbf{R} = \mathbf{I}$ , right plot). The figures depict a smoothed-out distribution (via kernel density estimators) of our input and output power spectra. To sample the distribution, we run 40 total injection levels, where the amplitude of  $\mathbf{e}$  is increased in even increments in log-space and ranges from  $P_{in} \sim -10^{13} mK^2(h^{-1}Mpc)^3$  (where one copy of  $\mathbf{e}$  in Equation (10) is negative and the other is positive) to  $P_{in} \sim 10^{13} mK^2(h^{-1}Mpc)^3$ . For each injection, we perform 20 bootstraps (over baselines, as explained in Section 3.2.2), resulting in a total of 800 data points on our  $P_{in}$  vs.  $P_{out}$  grid. It is noted that the transfer function is symmetric for negative and positive  $P_{in}$ 's, and so we fold all the values into positive ones to increase our signal-to-noise.

The solid black diagonal line in Figure 14 shows unity-transfer, or a perfect mapping from  $P_{out}$  to  $P_{in}$  (which we expect to occur for the unweighted case). The solid grey horizontal lines mark the peak of the data distribution  $\hat{\mathbf{p}}$  (the distribution is created from the 20 bootstraps) for both the inverse covariance weighted and unweighted cases. One can eyeball that a data value of  $10^5 mK^2(h^{-1}Mpc)^3$ , for example, would map approximately to a value of  $\sim 10^8 mK^2(h^{-1}Mpc)^3$  using the transfer curve for the inverse covariance weighted case, implying a signal loss factor of  $\sim 1000$ .

One peculiar aspect of Figure 14 is the fact that at low  $P_{in}$  values it appears that we can have signal gain ( $P_{out} > P_{in}$ ). This is unphysical in nature but caused due to the cross-terms dominating in Equation (13) once  $\mathbf{e}$  becomes small. As  $\mathbf{e}$  increases, we move into a regime where  $P_{out} \sim P_{in}$ , and then eventually into a regime where  $P_{out} < P_{in}$  when  $\mathbf{e}$  is large enough to be destroyed if weighting the data using itself. Although we only show figures for one  $k$  value, we note that the shape of the transfer curve is nearly identical for all  $k$ 's (though we treat each  $k$  separately).

Finally, it is worth thinking about the spread, or scatter, in our transfer curves in more detail. One might imagine that there should be one true  $P_{out}$  value for every  $P_{in}$ , implying one well-determined signal loss factor for every data value. In practice we have found that this is not the case, as evidenced by the colored 'heat-map' in Figure 14. The cause of this scatter can be thought

of as comprised of two components.

The first component is merely the fact that the values of the cross-terms in Equation (13) change for different EoR signals,  $\mathbf{e}$ . Since we draw different random  $\mathbf{e}$ 's for every bootstrap, there is a (small) range of  $P_{out}$  values that could result for the same  $P_{in}$ . This randomness is what causes the spread seen in the unweighted case (right plot of Figure 14), as well as most of the spread in the weighted case (left plot).

The second component of scatter is less intuitive and only applies (at a low level) to the weighted case. The origin of this scatter stems from how much the random EoR signal  $\mathbf{e}$  happens to look like the data  $\mathbf{x}$ . For example, if we are extremely unlucky,  $\mathbf{e}$  would have the same shapes, or eigenvectors, as  $\mathbf{x}$ . If weighting using empirically-derived covariances, this entire EoR signal would be destroyed. On the contrary, the less that  $\mathbf{e}$  looks like  $\mathbf{x}$ , the less signal loss that would result. This range of how 'unlucky' we can get is not that dramatic in real life, but it is important to correct for the fact that a particular  $P_{out}$  value could in principle stem from a range of  $P_{in}$  values.

We now explain how we use the transfer curves to map our data (a distribution along  $P_{out}$ ) to a signal-loss corrected distribution (along  $P_{in}$ ) that takes into account the range of signal loss that can be associated for a particular  $P_{out}$  value.

Beginning with smoothed probability distributions of the transfer function for the two cases (weighted and unweighted), we fit a polynomial to each, representing mean signal loss functions. We then account for the second component of scatter as described previously by de-convolving out  $P_{out,unweighted}$  from  $P_{out,weighted}$  for every  $P_{in}$  value. In other words, we only account for the extra scatter that the weighted case has over the unweighted case, which, as can be seen in Figure 14, is not large.

Equipped with our new signal loss curves (a one-to-one mapping function for the unweighted case, and a somewhat smeared out function for the weighted case), we multiply our data distribution  $\hat{\mathbf{p}}$  element-wise to all  $P_{in}$  columns, treating positive and negative halves of the data distribution separately. We note that for PAPER-64,  $\hat{\mathbf{p}}$  is sometimes narrowly peaked at positive power spectrum values (signifying detections of power), and sometimes centered around 0, representing noise-like measurements.

Finally, we sum up all rows of  $P_{out}$  where each row is a  $P_{in}$  probability distribution allowed by our measurements. This results in a final  $P_{in}$  distribution — the distribution of our data as seen through the signal loss lens. We show these final distributions in Figure 15 for every  $k$ . We compute power spectrum points from the peak of the histograms, and power spectrum errors from 95% confidence intervals.

To summarize this section, we also show power spectrum results for fringe-rate filtered PAPER-64 data before and after signal loss correction in Figure 16, using

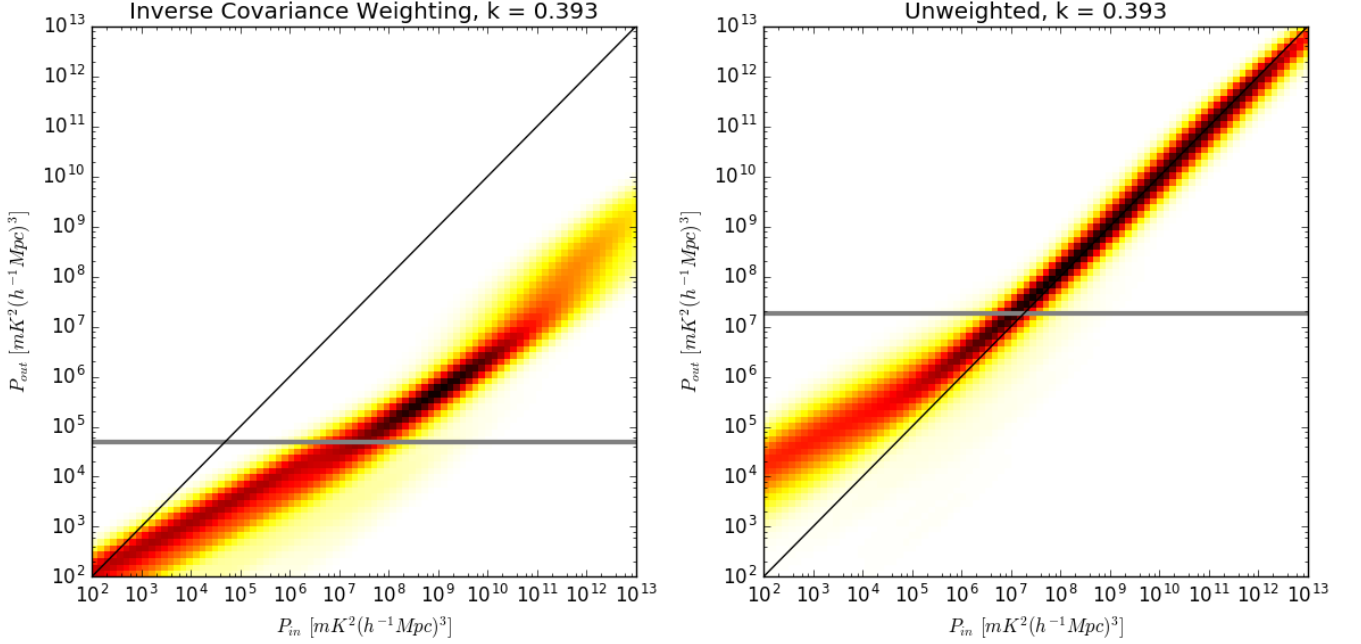


**Figure 14.** Signal loss transfer functions showing the relationship of  $P_{in}$  and  $P_{out}$ , as defined by Equations (10) and (11). Smoothed out distributions (via kernel density estimators) are shown as colored heat-maps for the cases of inverse covariance weighted PAPER-64 data (left) and unweighted data (right). The solid black diagonal line marks a perfect unity mapping, and the solid grey horizontal line denotes the peak of  $\hat{\mathbf{p}}$ , the data distribution. From these plots, it is clear that inverse covariance weighting results in  $\sim 3$  orders of magnitude of signal loss whereas the unweighted case does not exhibit loss.

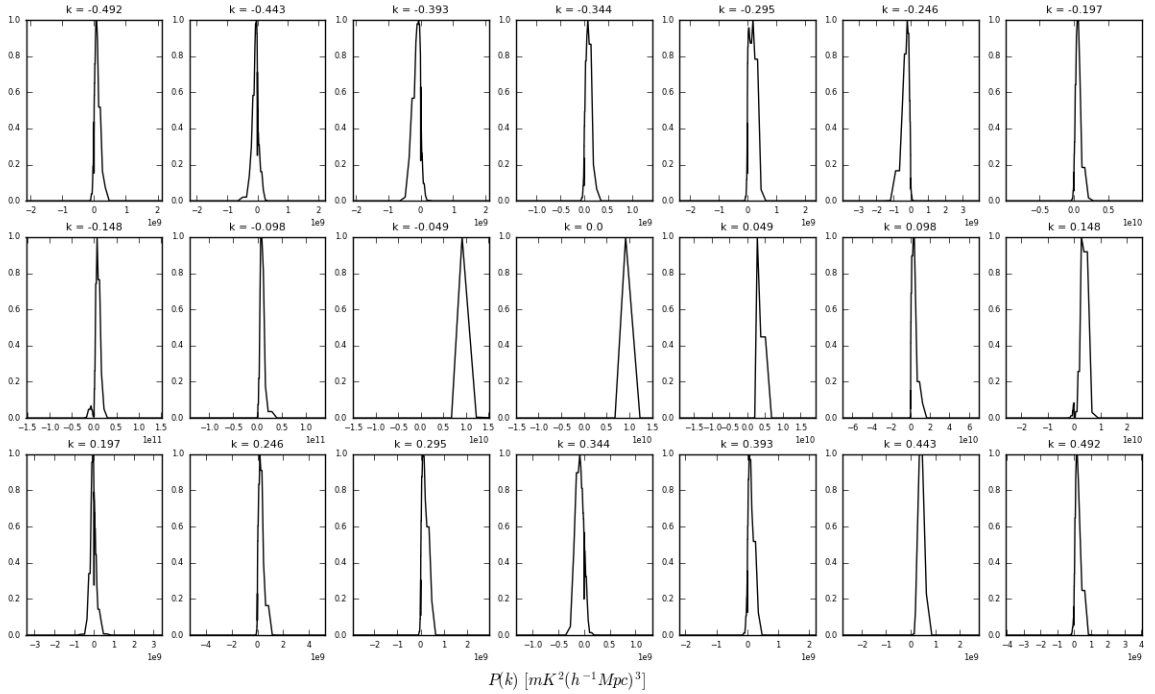


**Figure 15.** Normalized histograms of the power spectra that result from using inverse covariance weighting on PAPER-64 data after signal loss correction. Power spectrum points are computed from the peak of the distributions. Errors are computed using 95% confidence intervals.

inverse covariance weighting. The blue dashed line represents the unweighted power spectrum, which is identical in both panels (an important check, as we expect no signal loss for this case). The black and grey points are positive and negative power spectrum values plotted with  $2\sigma$  error bars. Prior to signal loss correction, it is clear that the power spectrum is unfeasible because it is well below the theoretical noise level prediction (solid green curve). Post-correction, the power spectrum values blow up to be higher than both the theory and unweighted power spectrum.

Investigating this further, the reason why the post-corrected power spectrum is so high is due to the small number of independent samples in PAPER-64. PAPER-64 has  $\sim 8$  independent modes after fringe-rate filtering while our power spectrum bandwidth has 21 channels. Consequently, the eigenvalues of  $\hat{\mathbf{C}}$  cannot possibly describe real fluctuations beyond the first 8. Hence, there is a substantial down-weighting of many random modes, a large loss that the signal loss transfer function captures and corrects for. **[CC: elaborate?]** In the next section, we investigate alternate weighting schemes to inverse covariance weighting, with the goal of finding one that balances the aggressiveness of down-weighting contaminants with minimizing the loss of EoR.

### 3.1.3. Minimizing Signal Loss

With our signal loss formalism established, we now have the capability of experimenting with different weighting options for  $\mathbf{R}$ . Our goal here is to choose a weighting method that successfully down-weights foregrounds and systematics in our data without generating large amounts of signal loss. We have found that the balance between the two is a delicate one and requires a careful understanding and altering of covariance matrices.

We saw in Section 2.1.3 how limiting the number of down-weighted eigenmodes (i.e. flattening out part of the eigenspectrum) can help minimize signal loss. We experiment with this idea on PAPER-64 data, dialing the number of modes down-weighted from zero (which is equivalent to identity-weighting, or the unweighted case) to 21 (which is full inverse covariance weighting of our 21 channels). The power spectrum results for one  $k$  value, both before and after signal loss correction, are shown in Figure 17. We see that the amount of signal loss increases as weighting becomes more aggressive (grey curve). In other words, more random fluctuations are being overfit and subtracted as more modes are down-weighted. We also find that the power spectrum upper limit, post signal loss correction, increases with the number of down-weighted modes (black curve). As discussed previously, we are limited in our power spectrum accuracy by the number of independent samples in our dataset and our errors dramatically increase as we surpass the  $\sim 8$  independent samples that we have in fringe-rate filtered PAPER-64 data.

Optimistically, we expect there to be a ‘sweet spot’ as we dial our regularization knob; a level of regularization

where weighting is beneficial compared to not weighting (blue dashed line). We see in Figure 17 that this occurs when only the strongest  $\sim 3$ -4 eigenmodes are down-weighted, though the improvement from the unweighted case is not significant.

Two additional horizontal lines are shown in Figure 17 which denote power spectrum values, post-signal loss correction, for two other regularization schemes. We multiply an identity matrix element-wise to  $\hat{\mathbf{C}}$  (i.e. inverse variance weighting, shown in red), and also add an arbitrary level of  $\mathbf{I}$  to  $\hat{\mathbf{C}}$  (cyan). We see that all three regularization schemes (black, red, cyan) perform similarly.

We choose to use  $\hat{\mathbf{C}} = \hat{\mathbf{C}}_{ij}\mathbf{I}_{ij}$ , or inverse variance weighting, for the remainder of this paper, which we will denote as  $\hat{\mathbf{C}}_{eff}$ . We choose this weighting scheme due to its simplicity in practice and because its effectiveness is comparable to other weighting schemes that produce minimal signal loss.

Our revised, best to-date PAPER-64 power spectrum (using only one baseline separation type) is shown in Figure 18. Again, black and grey points correspond to positive and negative power spectrum values respectively, with  $2\sigma$  errors bars. Also plotted are the unweighted power spectrum upper limit (dashed blue) and theoretical prediction of noise (solid green). From this result, we quote a best  $2\sigma$  upper limit of  $(158.0 \text{ mK})^2$  at  $k = 0.34 \text{ hMpc}^{-1}$ , a higher limit than Ali et al. (2015) by a factor of  $\sim 50$  in  $\text{mK}^2$  (though we only use one baseline type in our analysis as opposed to 3).

In this section we have shown three simple ways of regularizing  $\hat{\mathbf{C}}$  to minimize signal loss using PAPER-64 data. There are many other weighting schemes that we leave for consideration in future work. For example, one could estimate  $\hat{\mathbf{C}}$  using information from different subsets of baselines. For redundant arrays this could mean calculating  $\hat{\mathbf{C}}$  from a different but similar baseline type, such as the  $\sim 30 \text{ m}$  diagonal PAPER baselines (instead of the horizontal E/W ones). Alternately, covariances could be estimated from all other baselines except the two being cross-multiplied when forming a power spectrum estimate. This method was used in Parsons et al. (2014) in order to avoid suppressing the 21 cm signal, and it’s worth noting that the PAPER-32 results are likely safe from the issue of signal loss underestimation because of this very reason.

Another possible way to regularize  $\hat{\mathbf{C}}$  is to use information from different ranges of LST. For example, one could calculate  $\hat{\mathbf{C}}$  with data from LSTs where foregrounds are stronger (earlier or later LSTs than the ‘foreground-quiet’ range used in forming power spectra) — doing so may yield a better description of the foregrounds that we desire to down-weight. Fundamentally, each of these examples are similar in that they rely on a computation of  $\hat{\mathbf{C}}$  from data that is similar but not exactly the same as the data that is being down-weighted. Ideally this would be effective in down-weighting shared contaminants yet avoid signal loss from



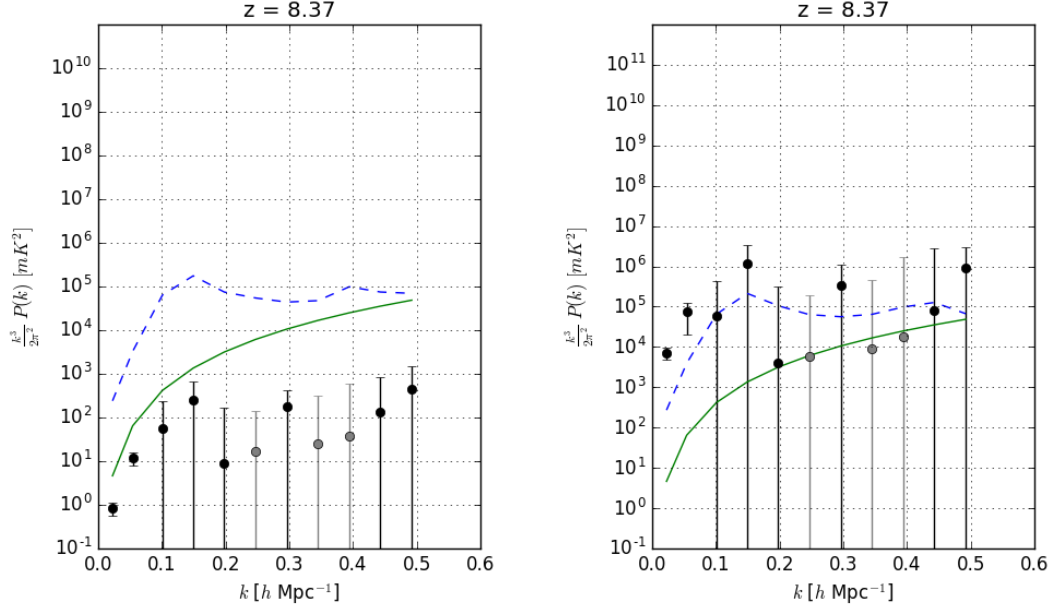


**Figure 16.** Full inverse covariance weighted power spectrum of PAPER-64 data (positive (black) and negative (grey) points, with  $2\sigma$  error bars) before signal loss correction (left) and after (right). The dashed blue line is the unweighted power spectrum ( $2\sigma$  upper limit). The solid green line is the theoretical noise level prediction based on observational parameters.

over-fitting modes in the power spectrum dataset itself.

### 3.2. PAPER-64: Error Estimation

In this section we discuss the ways in which we estimate errors for PAPER-64 power spectra. We first walk through a derivation for a theoretical error estimation (of thermal noise) based on observational parameters. Although a theoretical model often differs from true errors as explained in Section 2.2, it is helpful to understand the ideal case and the factors that affect its sensitivity. Additionally, we build on the lessons learned about bootstrapping in Section 2.2 to revise our bootstrapping method as applied to PAPER-64 data in order to compute accurate errors from the data itself.

In particular, we highlight major changes in both our sensitivity calculation and bootstrapping method that differ from the Ali et al. (2015) analysis of PAPER-64. While we do not discuss the changes within the context of PAPER-32, it is worth noting that the power spectrum results in Parsons et al. (2014) are affected by the same issues.

#### 3.2.1. Theoretical Error Estimation

Re-analysis of the PAPER-64 data included a detailed study using several independently generated noise simulations. What we found was that these simulations all agreed but were discrepant with the previous analytic sensitivity calculations. The analytic calculation is only an approximation, however the differences were large enough (factors of 10 in some cases) to warrant a careful investigation. The analytic calculation attempts to combine a large number of pieces of information in an approximate way, and when re-considering some of the

approximations we have found there to be large effects. What follows here is an accounting of the differences which have been discovered.

The sensitivity prediction [CC: need refs] for a power spectral analysis of interferometric 21 cm data, in temperature-units, is:

$$p(k) = \frac{X^2 Y \Omega_{eff} T_{sys}^2}{\sqrt{2 N_{lsts} N_{seps} t_{int} N_{days} N_{bls} N_{pols}}} \quad (16)$$

- $X^2 Y$ : Conversion factors from observing coordinates (angles on the sky) to cosmological coordinates (co-moving distances). For  $z = 8.4$ ,  $X^2 Y = 5 \times 10^{11} h^{-3} \text{Mpc}^3 \text{str}^{-1} \text{GHz}^{-1}$ .
- $\Omega_{eff}$ : The effective primary beam area in steradians<sup>2</sup>. The effective beam area changes with the application of a fringe-rate filter, since parts of the beam are up-weighted and down-weighted. Using numbers from Table 1 in Parsons et al. (2016),  $\Omega_{eff} = 0.74^2 / 0.24$  for an optimal fringe-rate filter.
- $T_{sys}$ : The system temperature is set by:

$$T_{sys} = 180 \left( \frac{\nu}{0.18} \right)^{-2.55} + T_{rcvr}, \quad (17)$$

where  $\nu$  are frequencies in GHz. We use a receiver temperature of 200 K, yielding  $T_{sys} = 487$  K

<sup>2</sup> [CC: ref equation]

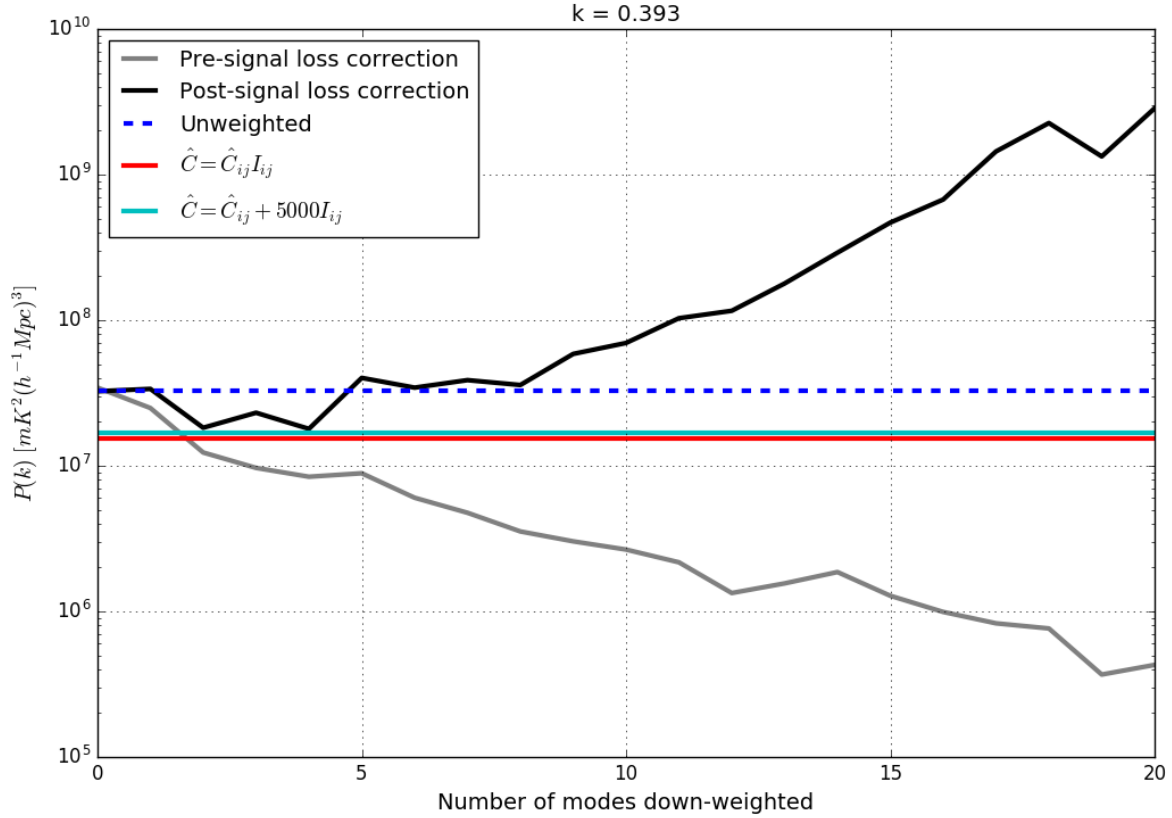


**Figure 17.** Power spectra  $2\sigma$  upper limits for  $k = 0.393$  for fringe-rate filtered PAPER-64 data. Values are shown before (grey) and after (black) signal loss correction as a function of number of eigenmodes of  $\hat{\mathbf{C}}$  that are down-weighted. This regularization knob is tuned from 0 modes (i.e. unweighted) to 21 modes (i.e. full inverse covariance weighting). Over  $\sim 3$  orders of magnitude of signal loss results when using inverse covariance weighting. Also plotted for comparison are  $2\sigma$  power spectrum upper limits for the unweighted case (dashed blue), inverse variance weighted case (red), and added-identity case (cyan). All three regularizations shown (black, red, cyan) perform similarly at their best.

150 MHz. This is lower than in Ali et al. (2015) because of previous failure to correct for using a median statistic.

- $\sqrt{2}$ : This factor in the denominator of the sensitivity equation comes from taking the real part of the power spectrum estimates after squaring visibility measurements. In Ali et al. (2015), a factor of 2 was mistakenly used.
- $N_{lsts}$ : The number of LST hours that go into a power spectrum estimation. The sensitivity scales as the square root because we integrate incoherently over time. For PAPER-64,  $N_{lsts} = 8$  hours.
- $N_{seps}$ : The number of baseline separation types averaged incoherently in a final power spectrum estimate. For the analysis in this paper, we only use one type of baseline, hence  $N_{seps} = 1$ . The revised limit in [CC: cite kolopanis paper] uses three separation types.
- $t_{int}$ : The integration time of the data. It is crucial to adapt this number if filtering is applied along

the time axis (i.e. a fringe-rate filter). We compute the effective integration time of our fringe-rate filtered data by scaling the original integration time using the following:

$$t_{frf} = t_{int} \frac{\int 1 df}{\int w^2(f) df}, \quad (18)$$

where  $t_{int} = 43$  seconds,  $t_{frf}$  is the fringe-rate filtered integration time,  $w$  is the fringe-rate profile, and the integral is taken over all fringe-rates. For PAPER-64, this number is  $t_{int} = 3857$  s.

- $N_{days}$ : The total number of days of data analyzed. In Ali et al. (2015), this number was set to 135. However, because we divide our data in half (to form ‘even’ and ‘odd’ datasets), this number should be reduced by a factor of 2. Additionally, because our LST coverage is not 100% complete (it doesn’t overlap for every single day), we compute a realistic value of  $N_{days}$  as:

$$\frac{1}{N_{days}} = \sqrt{\left\langle \frac{1}{N_i^2} \right\rangle_i}, \quad (19)$$

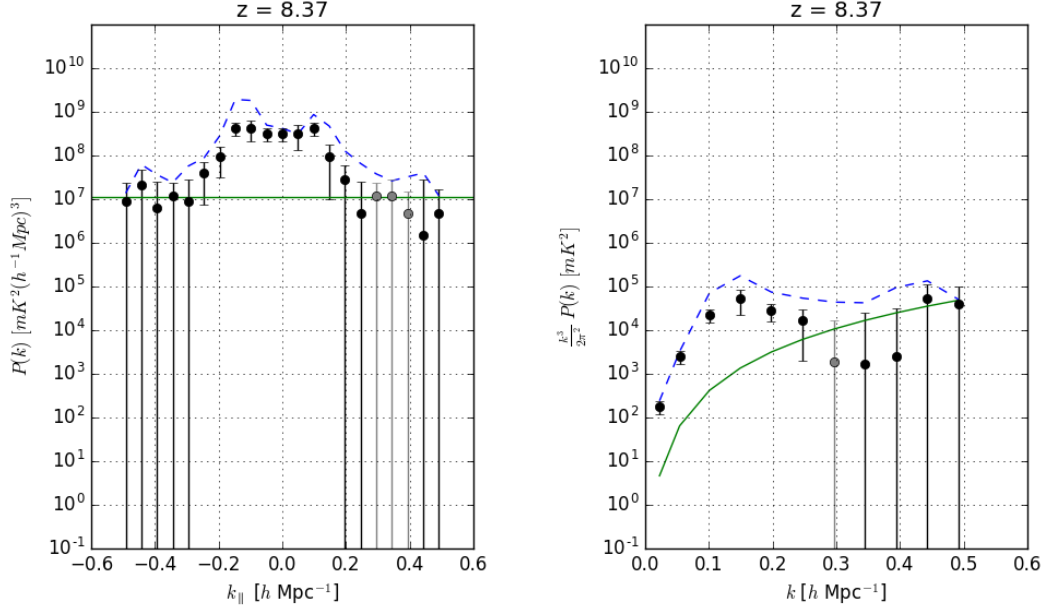


**Figure 18.** Highest sensitivity power spectrum of PAPER-64 using  $\hat{C}_{eff}$ . Black and grey points correspond to positive and negative power spectrum values, respectively, with  $2\sigma$  error bars also plotted. The dashed blue line is the unweighted power spectrum ( $2\sigma$  upper limit). The solid green line is the theoretical noise level prediction based on observational parameters. This power spectrum result differs from Ali et al. (2015) in that it only uses data from one type of baseline (30 m East/West baselines) instead of three. Additionally, an optimal fringe-rate filter was used instead of a degraded one, resulting in an increase in sensitivity but also an increase in signal loss. Major differences from previously published results stem from revisions regarding signal loss, bootstrapping, and the theoretical error computation. We quote a best  $2\sigma$  upper limit of  $(158.0 \text{ mK})^2$  at  $k = 0.34 \text{ hMpc}^{-1}$ , a higher limit than Ali et al. (2015) by a factor of  $\sim 50$  in  $\text{mK}^2$ .

where  $i$  is over LST (Jacobs et al. 2015). For PAPER-64, our revised estimate of  $N_{days}$  is  $\sim 34$  days.

- $N_{bls}$ : The number of baselines contributing to the sensitivity of a power spectrum estimate. In Ali et al. (2015), this number was the total number of 30 m East/West baselines used in the analysis. However, using the total number of baselines neglects the fact that baselines are averaged into groups before cross-multiplying data. Our revised estimate for the parameter is  $N_{bls} = \frac{N_{bls}}{N_{gps}} \sqrt{N_{gps}^2 - N_{gps}}$ , where, for the Ali et al. (2015) analysis,  $N_{gps} = 5$ . Each baseline group averages down linearly as the number of baselines entering the group ( $N_{bls}/N_{gps}$ ) and then as square root of the number of cross multiplied pairs ( $\sqrt{N_{gps}^2 - N_{gps}}$ ). For the revised PAPER-64 analysis with only one baseline separation type, this becomes  $N_{bls} \sim 46$ .
- $N_{pols}$ : The number of polarizations averaged together. For the case of Stokes I,  $N_{pols} = 2$ .

An additional factor of  $\sqrt{2}$  is gained in sensitivity when folding our power spectra into  $\Delta^2(k)$ , due to averaging together positive and negative  $k$ 's.

Our revised sensitivity estimate for PAPER-64 is shown in comparison with that of Ali et al. (2015) in

Figure 19. Together, the revised parameters yield a decrease in sensitivity (higher noise floor) by a factor of  $\sim 7$ . This is consistent with

To verify our thermal noise prediction, we form power spectra estimates using a pure noise simulation. We create Gaussian random noise assuming a constant  $T_{sys}$  (neglecting sky variation) but accounting for the true  $N_{days}$  as determined by LST sampling counts for each time and frequency in the LST-binned data. We convert  $T_{sys}$  into a variance statistic using:

$$T_{rms} = \frac{T_{sys}}{\sqrt{\Delta\nu\Delta t N_{days} N_{pols}}}, \quad (20)$$

where  $\Delta\nu$  is channel spacing,  $\Delta t$  is integration time,  $N_{days}$  is the number of daily counts for a particular time and frequency that went into our LST binned set, and  $N_{pols}$  is the number of polarizations (2 for Stokes I). This RMS temperature sets the variance of the Gaussian random noise.

Power spectrum results for the noise simulation are shown in Figure 20, where the black and grey points represent positive and negative power spectrum values, respectively (with  $2\sigma$  error bars and weighting matrix  $\hat{C}_{eff}$ ), the dashed blue line represents the unweighted power spectrum, and the solid green line denotes our  $2\sigma$  theoretical noise prediction as calculated by Equation (16). All three are in agreement, validating our analytical thermal noise calculation.

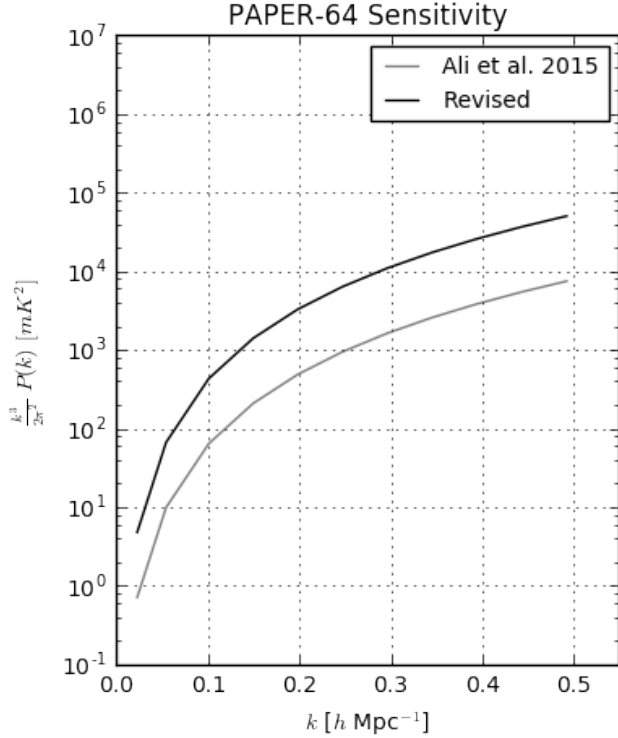


**Figure 19.** An updated prediction for the noise-level of PAPER-64 data (black) is shown in comparison to previously published sensitivity limits (grey). Both sensitivity analyses plotted assume only one baseline type (an additional factor of  $\sqrt{3}$  for 3 baseline types is needed to match Ali et al. (2015) exactly). Major factors that contribute to the discrepancy are  $\Omega_{eff}$ ,  $N_{days}$  and  $N_{bts}$ , as described in Section 3.2.1, which when combined decreases our sensitivity (higher noise floor) by a factor of  $\sim 7$ .

### 3.2.2. Bootstrapping

We bootstrap PAPER-64 power spectra in order to determine confidence intervals for our results. In this section, we highlight two major changes in the way we estimate errors since Ali et al. (2015), using the lessons we’ve learned about sampling with replacement and bootstrapping independent samples.

As discussed in Section 2.2, bootstrapping is only a valid way of estimating errors if a dataset is comprised of independent samples. The PAPER-64 pipeline outputs 20 bootstraps (over baselines), each a 2-dimensional power spectrum that is a function of  $k$  and time. In Ali et al. (2015), a second round of bootstrapping occurred over the baseline bootstrap and time axes simultaneously. Random values were sampled with replacement along both axes, drawing as many values as there are number of time integrations. Final power spectrum limits were then computed by taking the mean and standard deviation over this second bootstrap axis (which is typically large, on the order of  $N_{boot} \sim 400$ ). We emphasize that in this previous version, the number of elements sampled per bootstrap (number of times  $\sim 700$ ) greatly exceeds the number of independent LST samples, underestimating errors.

Because our dataset is fringe-rate filtered, we have substantially increased our integration time, resulting in fewer independent samples (from  $\sim 700$  samples to 8 samples). A random draw of 700 samples from this dataset therefore has many repeated samples, and the variance between hundreds ( $N_{boot}$ ) of these random samples is smaller than the true underlying variance of the data.

Given our new understanding of the sensitivity of bootstraps to the number of elements sampled, we have removed the second step entirely and now simply bootstrap over baselines with the “single replacement” strategy described in Section 2.2.

The single replacement strategy also provides a higher sensitivity estimate as only at most one baseline is repeated in each group. In Ali et al. (2015), baselines were chosen for groups randomly with replacement. In doing so,  $\sim 3$ -4 baselines per group were repeated (Figure 10 shows the fraction of independent samples to be  $\sim 55\%$  for 10 total independent samples) which sacrificed some sensitivity.

Power spectrum estimates with these bootstrapping changes for PAPER-64 fringe-rate filtered data are shown in Figure 21. The estimates are unweighted in order to disentangle the effects of bootstrapping from signal loss. As shown in the figure, when the baseline average includes many repeated samples the error is over-estimated, while when only one sample in the same average is allowed the possibility of being a repeat, the error on the noise-dominated higher  $k$  modes converges to the theoretical noise level. However, if more elements are drawn for each bootstrap than the number of independent samples (by drawing many times along the time axis), repeated values begin to crop up and the apparent variation between bootstraps drops, resulting in limits below the predicted noise level.

## 3.3. PAPER-64: Bias

In Section 2.3 we highlighted some common sources of bias that can show up as a power spectrum detection and imitate EoR. We discussed the importance of using jackknife and null tests for instilling confidence in an EoR detection, as well as identifying other sources of biases. Here we demonstrate methods used by PAPER-64 to mitigate foreground and noise bias and we perform jackknife and null tests in order to characterize the stability and implications of our results.

### 3.3.1. Mitigating Bias

We briefly discuss one way in which we mitigate foreground leakage in a power spectrum estimate, and two in which we suppress noise biases. These methods are not novel to this analysis but here we frame them in the context of minimizing false (non-EoR) detections.

Tailoring window functions is one way to suppress foreground biases. As alluded to in Section 2.1, we have a choice for the normalization matrix  $\mathbf{M}$  in Equation (2). For the analysis of PAPER-64 data, we compute



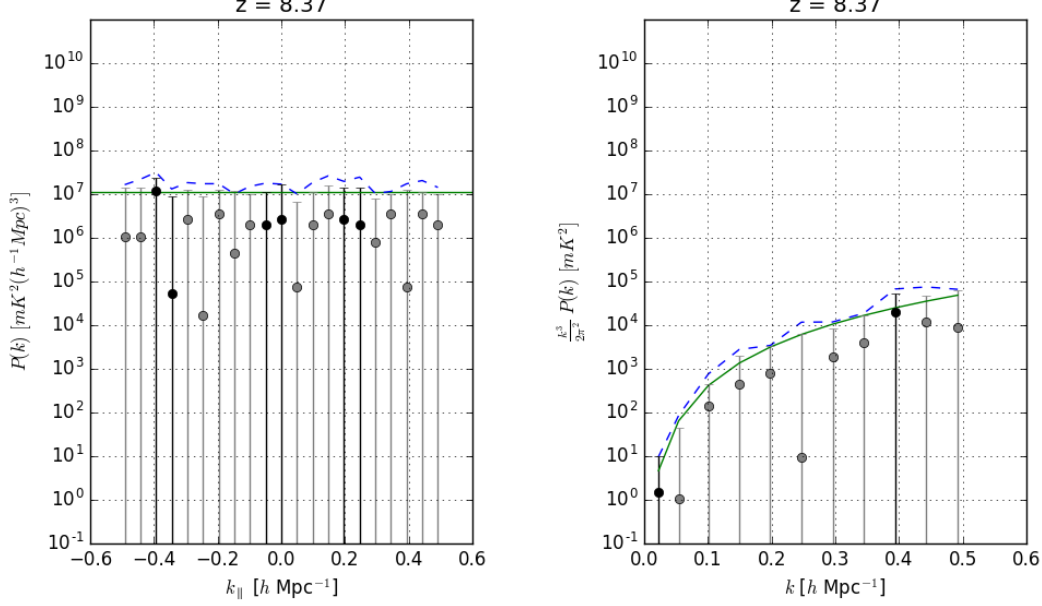


**Figure 20.** Power spectrum estimate for a noise simulation that mimics the noise level of PAPER-64 data. The weighted power spectrum points and  $2\sigma$  errors are shown in black and grey (positive and negative values), where we use  $\hat{\mathbf{C}}_{eff}$  to minimize signal loss. The dashed blue line is the unweighted power spectrum (also  $2\sigma$  upper limit). The solid green line is the theoretical noise level prediction as calculated by Equation (16). All three estimates agree.

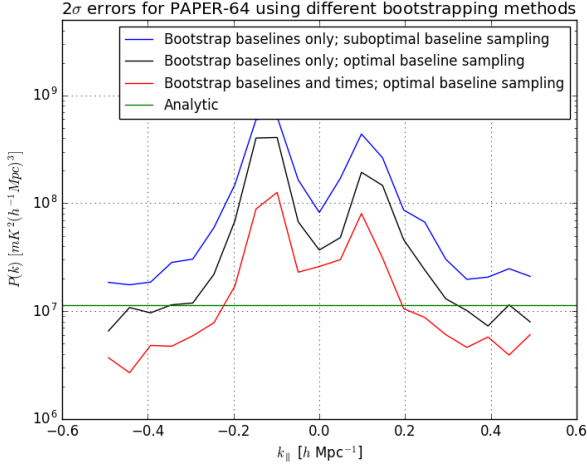


**Figure 21.**  $2\sigma$  power spectrum errors (not upper limits) using PAPER-64 data and three different bootstrapping methods. The data is fringe-rate filtered and a weighting matrix of  $\mathbf{I}$  (unweighted) is used in order to disentangle the effects of bootstrapping from signal loss. Three different bootstrapping methods are shown: the blue and black use methods where bootstrapping occurs on the baseline axis only (not the time axis), and they differ by how the baselines are randomly sampled. It is evident that sensitivity is maximized when baselines are sampled in a way that ensures mostly independent samples (only the last baseline spot is sampled randomly), as shown by the black curve. In red, bootstrapping occurs over both the baseline and time axes, illustrating how errors can be under-estimated if sampling more values than independent ones (fringe-rate filtering reduces the number of independent samples).

$\mathbf{M}$  using the Fisher matrix  $\mathbf{F}$ , defined as:

$$\mathbf{F}_{\alpha\beta} = \frac{1}{2} \text{tr}[\mathbf{R}\mathbf{Q}^\alpha \mathbf{R}\mathbf{Q}^\beta] \quad (21)$$

where  $\mathbf{R}$  is the data-weighting matrix and  $\alpha$  and  $\beta$  are wavebands in  $k_{\parallel}$ . We take the Cholesky decomposition of  $\mathbf{F}$ , decomposing it into two lower triangular matrices:

$$\mathbf{F} = \mathbf{L}\mathbf{L}^\dagger. \quad (22)$$

Next, we construct  $\mathbf{M}$ :

$$\mathbf{M} = \mathbf{D}\mathbf{L}^{-1} \quad (23)$$

where  $\mathbf{D}$  is a diagonal matrix. In doing so, our window function, defined as  $\mathbf{W} = \mathbf{M}\mathbf{F}$ , becomes:

$$\mathbf{W} = \mathbf{D}\mathbf{L}^\dagger. \quad (24)$$

Because of the nature of the lower triangular matrix, this window function has the property of preventing the leakage of foreground power from low  $k$  to high  $k$  modes. Specifically, we order the elements in  $\mathbf{F}$  in such a way so that power can leak from high  $k$  modes to low  $k$  modes, but not vice versa. Since most foreground power shows up at low  $k$ 's, this method ensures a window function that retains clean, noise-dominated measurements while minimizing the contamination of foreground bias.

In addition to mitigating foreground bias at high  $k$ 's, two other sources of bias that we actively suppress in the PAPER-64 analysis are noise bias associated with the squaring of thermal noise and noise bias from crosstalk. In order to avoid the former, we filter out

certain cross-multiplications when forming  $\hat{q}$  in Equation (1). Namely, the PAPER-64 dataset is divided into two halves: even julian dates and odd julian dates. Our data vectors are then  $\mathbf{x}_{even,1}$  for the ‘even’ dataset and baseline group 1,  $\mathbf{x}_{odd,1}$  for the ‘odd’ dataset and baseline group 1, etc. We only form  $\hat{q}$  when the two copies of  $\mathbf{x}$  come from different groups and baselines, never multiplying ‘even’ with ‘even’, for example, in order to prevent the squaring of the same thermal noise.

To mitigate crosstalk bias, which appears as a static bias in time, we apply a fringe-rate filter that suppresses fringe-rates of zero. Figure 13 shows that the filter response is zero for such static signals. The effect of filtering out zero fringe-rates on power spectrum results is shown in Ali et al. (2015). Most notably, power spectrum detections exist at all  $k$ ’s without crosstalk removal and these are detections that, depending on the power spectrum level, could be mistaken for EoR.

### 3.3.2. Jackknife Tests

The highest sensitivity power spectrum result using PAPER-64 data and all revised methods, shown in Figure 18, has positive biases at low  $k$  values. As discussed in Section 2.3.1, these detections are most likely attributable to foreground leakage. Here we demonstrate 3 null tests performed on PAPER-64 data that verify that the positive detections are indeed due to foreground variation and not attributable to EoR.

The 3 null test results are shown in Figure 22, with each test described as the following:

- Original (black): This is identical to the power spectrum in Figure 18 and represents the best revised PAPER-64 power spectrum (one baseline type only) with weighting matrix  $\mathbf{C}_{eff}$ . There are clear detections at low  $k$ ’s.
- Even/Odd (blue): We split our dataset into even (e) and odd (o) days, where  $\mathbf{x}_1 = e + o$  and  $\mathbf{x}_2 = e - o$ . We form datasets in this way to ensure that we use the full sensitivity of our data. When cross-multiplied, we obtain:

$$\mathbf{x}_1 \mathbf{x}_2^\dagger = ee^\dagger - eo^\dagger + oe^\dagger - oo^\dagger \quad (25)$$

If the same sky signal is in both the even and odd datasets, we expect it to cancel out.

- Baselines (green): We split our dataset into two halves, where each contains half of the total baselines used in the analysis. Again, we form  $\mathbf{x}_1 = b_1 + b_2$  and  $\mathbf{x}_2 = b_1 - b_2$ , where  $b_1$  is the first baseline group and  $b_2$  is the second baseline group.
- LST (purple): We split our dataset into two halves based on LST, namely  $t_1$  (LSTs 0.5-4.6 hours) and  $t_2$  (LSTs 4.6-8.6 hours). We form our two datasets as  $\mathbf{x}_1 = t_1 + t_2$  and  $\mathbf{x}_2 = t_1 - t_2$

Investigating Figure 22, we find that both the baselines and even/odd null tests are consistent with noise.

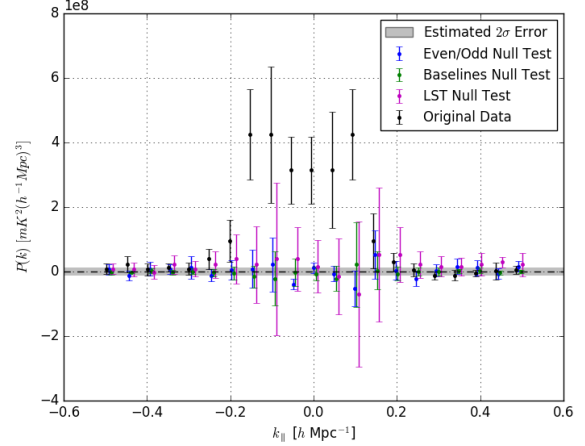


**Figure 22.** Results of 3 null tests compared to the PAPER-64 revised power spectrum (black) and estimated  $2\sigma$  errors (grey shaded region). For each, we took jackknives along different axes of the dataset - by julian days (separating even and odd days; blue), by baselines (green), and by LST (purple). We expect the sky signal to disappear for a ‘passing’ null test. We find that the biases in our power spectrum are likely caused by variation of foregrounds in LST, and are not attributable to particular baselines or days of data.

We note that the error bars for the baselines test (green) are especially small — this is because the signal is effectively cancelled out prior to cross-multiplication (when forming baseline groups).

The null test in LST (purple) is much more illuminating. The fact that there are many power spectrum points outside the estimated error region signifies that the bias we see is likely from foregrounds that vary in LST. In other words,  $t_1$  and  $t_2$  differ by an amount greater than thermal noise and they do not effectively cancel out the sky signal during cross-multiplication. The errors on this null test are also large, also reflective of residual foregrounds.

We do not investigate the detailed nature of the residual foregrounds in this paper, though one could imagine performing many similar null tests with a sliding window of  $t_1$ ’s and  $t_2$ ’s. This would illuminate the particular LST range that introduces the foreground bias (or whether the bias is constant in LST), and could potentially be traced to a individual bright radio source. This type of detailed analysis will be critical at EoR sensitivities, however, for the purpose of this paper we are not surprised that the bias we see comes from foregrounds in regions where we expect leakage.

## 4. CONCLUSION

Although current 21 cm published power spectrum upper limits lie a  $\sim$ couple orders of magnitude above predicted EoR levels, ongoing analyses of deeper sensitivity datasets from PAPER, MWA, and LOFAR, as well as next generation instruments like HERA, expect to continue to push towards EoR sensitivities. As the field progresses towards a coveted detection, we have shown that it is crucial for future analyses to have a rigorous under-

standing of signal loss in an analysis pipeline, be able to accurately and robustly calculate both power spectrum and theoretical errors, and consistently undergo a comprehensive set of jackknife and null tests.

In particular, in this paper we have investigated the subtleties and tradeoffs of common 21 cm power spectrum techniques on signal loss, error estimation, and bias, which can be summarized as follows:

- Substantial signal loss can result when weighting data using empirically estimated covariances. Loss of the 21 cm signal is especially significant if more eigenmodes are down-weighted than exist in the data (having an under-constrained covariance matrix). Hence, there exists a trade-off between sensitivity driven time-averaging techniques such as fringe-rate filtering and signal loss.
- Signal injection and recovery simulations can be used to quantify signal loss. However, a signal-only simulation can underestimate loss by failing to account for spurious correlations between the data and signal.
- Errors that are estimated via bootstrapping can be underestimated if samples in the dataset are correlated. If the number of independent samples in a dataset is well-determined, bootstrapping is a simple and accurate way of estimating errors.
- An EoR detection must pass all null tests. Similarly, performing jackknife tests along multiple axes of a dataset is necessary for confidence in a true EoR detection, and can also be used to tease out systematics.

As a consequence of our investigations, we have also revised power spectrum results from PAPER-64. For an analysis of only one baseline type, we quote a new  $2\sigma$  upper limit of  $(158.0 \text{ mK})^2$  at  $k = 0.34 \text{ hMpc}^{-1}$ , a higher limit than Ali et al. (2015) by a factor of  $\sim 50$  in  $\text{mK}^2$ . The reasons for a previously underestimated limit and ways in which our new analysis differs can be summarized by the following:

- Signal loss, previously found to be  $< 2\%$  in Ali et al. (2015), was underestimated by a factor of  $\sim 1000$ . Because PAPER-64 is limited by its number of samples, we use a regularized covariance weighting in our revised analysis to minimize loss, thereby increasing the original PAPER-64 limit in  $\text{mK}^2$  by a factor of  $\sim 50$  instead of 1000. Underestimated signal loss represents the bulk of our revision.

- Power spectrum errors, originally computed by bootstrapping, were underestimated by a factor of  $\sim 2$  due to oversampling data with a reduced number of independent samples from fringe-rate filtering. They were also overestimated by a factor of  $\sim 2$  from using a suboptimal way of combining baselines into groups when forming power spectra. Hence, the net change for our error estimation is negligible, though the intuition behind the previous estimation was incorrect.
- Several factors used in an analytic expression to predict the noise-level in PAPER-64 data were revised, yielding an increase in predicted sensitivity level by a factor of  $\sim 7$ . We have verified our revised prediction extensively using pure noise simulations.

The 21 cm future is exciting, as new experiments have sensitivities that expect to reach and surpass EoR levels, improved foreground mitigation/removal strategies are being developed, and simulations are being designed to better understand instruments. On the power spectrum analysis side, we recognize that there is still much work to do. Even with robust signal loss simulations and precise error calculations, we are currently limited by data volume and foreground suppression strategies. However, the future promises to bring higher sensitivity 21 cm measurements, better foreground and instrumental models, more effective and less lossy weighting techniques — and with all that, an improved understanding of reionization and our early Universe.

## 5. ACKNOWLEDGEMENTS

The author would like to acknowledge the UC Berkeley Chancellor’s Fellowship, National Science Foundation Graduate Research Fellowship (Division of Graduate Education award 1106400), and thank Eric Switzer for helpful discussions. PAPER is supported by grants from the National Science Foundation (awards 0804508, 1129258, and 1125558). ARP, JCP, and DCJ would also like to acknowledge NSF support (awards 1352519, 1302774, and 1401708, respectively). JEA would like to acknowledge a generous grant from the Mount Cuba Astronomical Association for computing resources. We also graciously thank SKA-SA for site infrastructure and observing support.

## APPENDIX

### A. A TOY MODEL FOR SIGNAL LOSS

[CC: Note to Adrian: I standardized all Q indices to be superscripts instead of subscripts. Also standardized equations to be “Equation eqref” (spell out Equation, and use eqref for references)]

In this Appendix, we examine a toy model for signal loss. Our goal is to build intuition by deriving an analytic formula for power spectrum signal loss. We will also show that in general, signal loss appears as a multiplicative bias on one's power spectrum estimate.

The minimum-variance quadratic estimator  $\hat{p}_\alpha$  for the  $\alpha$ th bandpower of the power spectrum is given by [ACL: Also need to state in a footnote that for this section only we'll assume without loss of generality that the data are real]

$$\hat{p}_\alpha = \frac{1}{2\mathbf{F}_{\alpha\alpha}} \mathbf{x}^t \mathbf{C}^{-1} \mathbf{Q}^\alpha \mathbf{C}^{-1} \mathbf{x}, \quad (\text{A1})$$

where

$$F_{\alpha\alpha} \equiv \frac{1}{2} \text{tr} (\mathbf{C}^{-1} \mathbf{Q}^\alpha \mathbf{C}^{-1} \mathbf{Q}^\alpha) \quad (\text{A2})$$

is the  $\alpha$ th diagonal element of the Fisher matrix. In our case, however, we do not have *a priori* knowledge of the covariance matrix. Thus, we replace  $\mathbf{C}$  with  $\hat{\mathbf{C}}$ , its data-derived approximation. Our estimator then becomes

$$\hat{p}_\alpha^{\text{loss}} = \frac{1}{2\hat{\mathbf{F}}_{\alpha\alpha}} \mathbf{x}^t \hat{\mathbf{C}}^{-1} \mathbf{Q}^\alpha \hat{\mathbf{C}}^{-1} \mathbf{x}, \quad (\text{A3})$$

where

$$\hat{\mathbf{F}}_{\alpha\alpha} \equiv \frac{1}{2} \text{tr} (\hat{\mathbf{C}}^{-1} \mathbf{Q}^\alpha \hat{\mathbf{C}}^{-1} \mathbf{Q}^\alpha), \quad (\text{A4})$$

with the label “loss” to foreshadow the fact that this will be an estimator with signal loss (i.e., a multiplicative bias of less than unity). We will now provide an explicit demonstration of this by modeling the estimated covariance as

$$\hat{\mathbf{C}} = (1 - \eta) \mathbf{C} + \eta \mathbf{x} \mathbf{x}^t, \quad (\text{A5})$$

where  $\eta$  is parameter quantifying our success at estimating the true covariance matrix. If  $\eta = 0$ , our covariance estimate has perfectly modeled the true covariance and  $\hat{\mathbf{C}} = \mathbf{C}$ . On the other hand, if  $\eta = 1$ , then our covariance estimate is based purely on the one realization of the covariance that is our actual data, and we would expect a high level of overfitting and signal loss.

Our strategy for computing the signal loss will be to insert Equation (A5) into Equation (A3) and to express the resulting estimator  $\hat{p}_\alpha^{\text{loss}}$  in terms of  $\hat{p}_\alpha$ . We begin by expressing  $\hat{\mathbf{C}}^{-1}$  in terms of  $\mathbf{C}^{-1}$  using the Woodbury identity so that

$$\hat{\mathbf{C}}^{-1} = \frac{\mathbf{C}^{-1}}{1 - \eta} \left[ \mathbf{I} - \frac{\eta \mathbf{x} \mathbf{x}^t \mathbf{C}^{-1}}{1 + \eta(g - 1)} \right], \quad (\text{A6})$$

where we have defined  $g \equiv \mathbf{x}^t \mathbf{C}^{-1} \mathbf{x}$ . Inserting this into our Fisher estimate we have

$$\hat{\mathbf{F}}_{\alpha\alpha} = \frac{F_{\alpha\alpha}}{(1 - \eta)^2} \left[ 1 - \frac{\eta}{1 + \eta(g - 1)} \frac{h_{\alpha\alpha}}{F_{\alpha\alpha}} + \frac{1}{2} \left( \frac{\eta}{1 + \eta(g - 1)} \right)^2 \frac{h_\alpha^2}{F_{\alpha\alpha}} \right], \quad (\text{A7})$$

where  $h_\alpha \equiv \mathbf{x}^t \mathbf{C}^{-1} \mathbf{Q}^\alpha \mathbf{C}^{-1} \mathbf{x}$  and  $h_{\alpha\alpha} \equiv \mathbf{x}^t \mathbf{C}^{-1} \mathbf{Q}^\alpha \mathbf{C}^{-1} \mathbf{Q}^\alpha \mathbf{C}^{-1} \mathbf{x}$ . Note that  $g$ ,  $h_\alpha$ , and  $h_{\alpha\alpha}$  are all random variables, since they depend on  $\mathbf{x}$ . Inserting these expressions into our estimator gives

$$\begin{aligned} \hat{p}_\alpha^{\text{loss}} &= \frac{1}{2} \frac{h_\alpha}{F_{\alpha\alpha}} \left[ 1 - \frac{\eta g}{1 + \eta(g - 1)} \right]^2 \left[ 1 - \frac{\eta}{1 + \eta(g - 1)} \frac{h_{\alpha\alpha}}{F_{\alpha\alpha}} + \frac{1}{2} \left( \frac{\eta}{1 + \eta(g - 1)} \right)^2 \frac{h_\alpha^2}{F_{\alpha\alpha}} \right]^{-1} \\ &= \frac{1}{2} \frac{h_\alpha}{F_{\alpha\alpha}} (1 - 2\beta + \beta^2) \sum_{n=0}^{\infty} \sum_{k=0}^n \binom{n}{k} \left( \frac{\varepsilon h_{\alpha\alpha}}{F_{\alpha\alpha}} \right)^k \left( -\frac{\varepsilon^2 h_\alpha^2}{2F_{\alpha\alpha}} \right)^{n-k}, \end{aligned} \quad (\text{A8})$$

where  $\beta \equiv \eta g / [1 + \eta(g - 1)]$  and  $\varepsilon \equiv \beta / g$ . To proceed, we take the ensemble average of  $\hat{p}_\alpha^{\text{loss}}$  to understand its average statistical properties. Inspecting Equation (A8), we see that its expectation value is a linear sum of terms of the form  $\langle \beta^a h_\alpha^b h_{\alpha\alpha}^c \varepsilon^d \rangle$ , where  $a$ ,  $b$ , and  $c$  are integers. Expanding  $\beta$  in powers of  $g$ , we have

$$\langle \beta^a h_\alpha^b h_{\alpha\alpha}^c \varepsilon^d \rangle = \sum_{m_1=1}^{\infty} \cdots \sum_{m_{a+d}=1}^{\infty} \frac{(-\eta)^{m_1+\cdots+m_{a+d}}}{(1 - \eta)^{m_1+\cdots+m_a}} \langle g^{m_1+\cdots+m_{a+d}-d} h_\alpha^b h_{\alpha\alpha}^c \rangle. \quad (\text{A9})$$



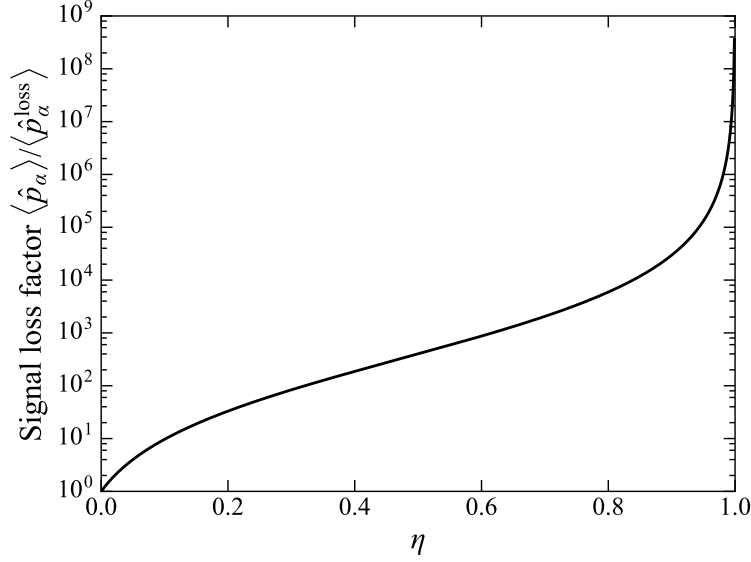


**Figure A1.** Power spectrum signal loss for  $N = 20$  for a toy model where  $\hat{\mathbf{C}} = (1 - \eta)\mathbf{C} + \eta\mathbf{x}\mathbf{x}^t$ .

Writing out the ensemble averaged quantity on the right hand side and defining  $M \equiv m_1 + \dots + m_{a+d}$  yields

$$\begin{aligned} \langle g^{m_1 + \dots + m_{a+d}} h_\alpha^b h_{\alpha\alpha}^c \rangle &= \langle (\mathbf{x}^t \mathbf{C}^{-1} \mathbf{x})^M (\mathbf{x}^t \mathbf{C}^{-1} \mathbf{Q}^\alpha \mathbf{C}^{-1} \mathbf{x})^b (\mathbf{x}^t \mathbf{C}^{-1} \mathbf{Q}^\alpha \mathbf{C}^{-1} \mathbf{Q}^\alpha \mathbf{C}^{-1} \mathbf{x})^c \rangle \\ &= \sum_{i_1}^N \sum_{j_1}^N \dots \sum_{k_1}^N \sum_{l_1}^N \dots \sum_{p_1}^N \sum_{q_1}^N \dots (\mathbf{C}^{-1} \mathbf{Q}^\alpha \mathbf{C}^{-1} \mathbf{Q}^\alpha \mathbf{C}^{-1})_{p_1 q_1} \dots (\mathbf{C}^{-1} \mathbf{Q}^\alpha \mathbf{C}^{-1} \mathbf{Q}^\alpha \mathbf{C}^{-1})_{p_c q_c} \\ &\quad \times (\mathbf{C}^{-1} \mathbf{Q}^\alpha \mathbf{C}^{-1})_{k_1 l_1} \dots (\mathbf{C}^{-1} \mathbf{Q}^\alpha \mathbf{C}^{-1})_{k_b l_b} \mathbf{C}_{i_1 j_1}^{-1} \dots \mathbf{C}_{i_M j_M}^{-1} \langle x_{i_1} x_{j_1} \dots x_{k_1} x_{l_1} \dots x_{p_1} x_{q_1} \dots \rangle \end{aligned} \quad (\text{A10})$$

where  $N$  is the length of vector  $\mathbf{x}$ , i.e., the number of data points. To further simplify this expression, we assume that the data are Gaussian distributed. The expectation value on the right hand side can then be reduced to a sum of product of covariances, where each term in the sum is comprised of a particular way to partition the copies of  $x$  into pairs. However, in the limit of large  $N$  one particular partitioning dominates, and the result can be approximated as **[ACL: Should probably explain this more fully]**

$$\langle g^{m_1 + \dots + m_{a+d}} h_\alpha^b h_{\alpha\alpha}^c \rangle \approx N^{m_1 + \dots + m_{a+d}} [\text{tr}(\mathbf{C}^{-1} \mathbf{Q}^\alpha)]^b (2F_{\alpha\alpha})^c, \quad (\text{A11})$$

and re-inserting this into Equation (A9) yields

$$\langle \beta^a h_\alpha^b h_{\alpha\alpha}^c \varepsilon^d \rangle \approx \left[ \frac{\eta N}{1 + \eta(N-1)} \right]^a \left[ \frac{\eta}{1 + \eta(N-1)} \right]^d [\text{tr}(\mathbf{C}^{-1} \mathbf{Q}^\alpha)]^b (2F_{\alpha\alpha})^c. \quad (\text{A12})$$

With this result, taking the ensemble average of Equation (A8) is relatively straightforward. One simply replaces every copy of  $\beta$  with  $\beta_N \equiv \eta N / [1 + \eta(N-1)]$ , every copy of  $\varepsilon$  with  $\varepsilon_N \equiv \eta / [1 + \eta(N-1)]$ , every copy of  $h_\alpha$  with  $\text{tr}(\mathbf{C}^{-1} \mathbf{Q}^\alpha)$ , and every copy of  $h_{\alpha\alpha}$  with  $2F_{\alpha\alpha}$ . Performing these substitutions and recalling **[ACL: make sure the reader will indeed be recalling at this point]** that  $\langle \hat{p}_\alpha \rangle = \langle h_\alpha \rangle / 2F_{\alpha\alpha}$ , we obtain

$$\frac{\langle \hat{p}_\alpha \rangle}{\langle \hat{p}_\alpha^{\text{loss}} \rangle} = \frac{1 - 2\varepsilon_N + \varepsilon_N^2 [\text{tr}(\mathbf{C}^{-1} \mathbf{Q}^\alpha)]^2 / 2F_{\alpha\alpha}}{(1 - \beta_N)^2}. \quad (\text{A13})$$

This quantity is in general less than unity, and quantifies the signal loss relative to the ideal estimator  $\hat{p}_\alpha$  where we know the true covariance  $\mathbf{C}$ . As an illustrative example, for cases where  $\mathbf{C} \propto \mathbf{I}$ , this reduces to

$$\left. \frac{\langle \hat{p}_\alpha \rangle}{\langle \hat{p}_\alpha^{\text{loss}} \rangle} \right|_{\mathbf{C} \propto \mathbf{I}} = \left( \frac{1 - \varepsilon_N}{1 - \beta_N} \right)^2 = \left[ \frac{1 + \eta(N-2)}{1 - \eta} \right]^2. \quad (\text{A14})$$

This is shown in Figure A1 for  $N = 20$ . As expected, the signal loss factor is unity for  $\eta = 0$  (perfect estimation of  $\mathbf{C}$ ) and goes to infinity as  $\eta$  approaches 1.

In general, one’s estimate of the covariance will not be expressible in the form given by Equation (A5). However, the qualitative point here is that the signal loss can be expressed as a multiplicative factor. Even if  $\hat{\mathbf{C}}$  is more complicated than the form used for this toy model, the same mathematical technique of expressing the estimator as a series of higher-point functions, reducing these functions (assuming Gaussianity) to two-point functions, and re-summing any power series will show that the signal loss is a multiplicative factor. **[ACL: I can express this last bit more eloquently, but it’s late and I’m tired and need to eat dinner.]**

## REFERENCES

- Ali, Z. S., et al. 2015, *ApJ*, 809, 61
- Bond, J. R., Jaffe, A. H., & Knox, L. 1998, *PhRvD*, 57, 2117
- Bowman, J. D., & Rogers, A. E. E. 2010, *Nature*, 468, 796
- Burns, J. O., et al. 2012, *Advances in Space Research*, 49, 433
- Datta, A., Bowman, J. D., & Carilli, C. L. 2010, *The Astrophysical Journal*, 724, 526
- DeBoer, D. R., et al. 2017, *Publications of the Astronomical Society of the Pacific*, 129, 045001
- Ellingson, S. W., Clarke, T. E., Cohen, A., Craig, J., Kassim, N. E., Pihlstrom, Y., Rickard, L. J., & Taylor, G. B. 2009, *IEEE Proceedings*, 97, 1421
- Greenhill, L. J., & Bernardi, G. 2012, *ArXiv e-prints*
- Jacobs, D. C., et al. 2015, *ApJ*, 801, 51
- Keating, G. K., Marrone, D. P., Bower, G. C., Leitch, E., Carlstrom, J. E., & DeBoer, D. R. 2016, *The Astrophysical Journal*, 830, 34
- Liu, A., Parsons, A. R., & Trott, C. M. 2014a, *PhRvD*, 90, 023018
- . 2014b, *PhRvD*, 90, 023019
- Liu, A., & Tegmark, M. 2011, *Phys. Rev. D*, 83, 103006
- Paciga, G., et al. 2013, *MNRAS*
- Parsons, A. R., Liu, A., Ali, Z. S., & Cheng, C. 2016, *ApJ*, 820, 51
- Parsons, A. R., Pober, J. C., Aguirre, J. E., Carilli, C. L., Jacobs, D. C., & Moore, D. F. 2012, *ApJ*, 756, 165
- Parsons, A. R., et al. 2010, *AJ*, 139, 1468
- . 2014, *ApJ*, 788, 106
- Patra, N., Subrahmanyam, R., Sethi, S., Udaya Shankar, N., & Raghunathan, A. 2015, *ApJ*, 801, 138
- Peterson, U.-L. P. X.-P. W. J. 2004, *ArXiv Astrophysics e-prints*
- Pober, J. C., et al. 2013, *AJ*, 145, 65
- . 2014, *ApJ*, 782, 66
- Sokolowski, M., et al. 2015, *PASA*, 32, e004
- Switzer, E. R., Chang, T.-C., Masui, K. W., Pen, U.-L., & Voytek, T. C. 2015, *The Astrophysical Journal*, 815, 51
- Tegmark, M. 1997, *PhRvD*, 55, 5895
- Thyagarajan, N., et al. 2013, *ApJ*, 776, 6
- Tingay, S. J., et al. 2013, *PASA*, 30, 7
- van Haarlem, M. P., et al. 2013, *A&A*, 556, A2
- Vedantham, H., Shankar, N. U., & Subrahmanyam, R. 2012, *The Astrophysical Journal*, 745, 176
- Voytek, T. C., Natarajan, A., Jáuregui García, J. M., Peterson, J. B., & López-Cruz, O. 2014, *ApJL*, 782, L9
- Wu, X. 2009, in *Bulletin of the American Astronomical Society*, Vol. 41, American Astronomical Society Meeting Abstracts #213, 474